Catena 219 (2022) 106612

Contents lists available at ScienceDirect

Catena

journal homepage: www.elsevier.com/locate/catena

Application of induced polarization imaging across different scales to understand surface and groundwater flow at the Hofermuehle landslide

Adrian Flores Orozco *, Matthias Steiner, Timea Katona, Nathalie Roser, Clemens Moser, Margherita J. Stumvoll, Thomas Glade

TU Wien, Department of Geodesy and Geoinformation, Research Unit of Geophysics, 1040-Vienna, Austria
University of Vienna, Department of Geography and Regional Research, 1010-Vienna, Austria

ARTICLE INFO

Keywords:
Geophysics
Hydraulic conductivity
Hydrogeology
Landslide
Drainage
Water flow
Groundwater

ABSTRACT

Understanding changes in hydraulic properties of the subsurface is critical to delineate areas susceptible for groundwater accumulation and the triggering of landslides. Laboratory studies have demonstrated the possibility to estimate the hydraulic conductivity from induced polarization (IP) measurements. However, to-date only rare studies have been applied at the field scale and none has evaluated the frequency-dependence in field IP imaging data. We show that the application of petrophysical models linking hydraulic conductivity (K) and IP at 1 Hz, resolves for the same estimations from frequency-domain measurements as well as from time-domain IP. Moreover, our IP images reveal an evident frequency-dependence between 0.1 and 240 Hz in the electrical properties, which is also observed in lab measurements conducted in soil samples. To account for this, we fit a Cole-Cole model to our multi-frequency IP results and evaluate models linking K and the normalized chargeability, gaining a subsurface model of the hydraulic conductivity with enhanced resolution. Our results reveal clear variations at depth in the electrical conductivity and polarization associated with the presence of a plane of instability and the sliding plane. We also resolve lateral changes delineating areas with K below 10^{-6} m/s, which may act as barriers for groundwater flow. To evaluate our results we also estimate the hydraulic conductivity using a joint inversion algorithm that directly solves for porosity and saturation through the simultaneous inversion of seismic refraction and electrical resistivity tomography data. We observed consistent hydraulic conductivity images obtained through the inversion of the IP data and the joint inversion, with such model being in agreement with existing information of the site. We resolve a 3D model of the hydraulic conductivity at the Hofermuehle landslide from IP data that reveals the geometry of areas with poor drainage that may lead to land sliding.

1. Introduction

Landslide processes are of high interest due to their impact on infrastructure, human life and property as well as their role in landscape development. Clay-rich materials are especially prone to shallow and deep sliding processes (Lacroix et al., 2020; Sidle and Ochiai, 2006). In Austria, such mass mobilizations are typical for clay-rich materials corresponding to the Flysch- and Klippen zone at the northern fringe of the Eastern Alps (e.g., Damm and Terhorst, 2010; Bell et al., 2013; Petschko et al., 2013; Promper and Glade, 2016; Steger et al., 2016; Lima et al., 2017; Gallistl et al., 2018; Stumvoll et al., 2020). Landslides in clay-rich areas are mainly triggered by changes in groundwater level (see Lacroix et al., 2020 for a review), and are thus controlled by recharge (i.e., following precipitation and snowmelt) and by the hydraulic properties of the subsurface. The Hofermuehle landslide, located in the Flysch Zone of Lower Austria, is exemplary for landslide processes in the region. Both slow earth (sliding) movements coupled with fast earth flow processes can occur, characterizing it as a complex landslide (see Stumvoll et al., 2021; 2022 and references therein). Landslide processes at the site are complex also in terms of their behavior, with non-linear processes varying in space and time regarding location, volume of mobilized material, duration and velocity (Stumvoll et al., 2022).

The study area has been thoroughly investigated by means of direct methods, such as terrestrial and airborne laser scanning (TLS and ALS), dynamic probing, analysis of soil samples recovered from core drilling and the monitoring of a piezometer network (for details see Stumvoll

* Corresponding author at: TU Wien, Department of Geodesy and Geoinformation, Research Unit of Geophysics.
E-mail address: flores@geo.tuwien.ac.at (A. Flores Orozco).

https://doi.org/10.1016/j.catena.2022.106612
Received 3 February 2022; Received in revised form 20 August 2022; Accepted 29 August 2022
Available online 7 September 2022

et al., 2021; 2022). On the one hand, such studies have gained detailed information about the rates of surface deformation at different positions of the catchments, evidencing that there is probably more than one sliding plane, with shallow planes (at a depth between 2 and 3 m) being likely interconnected. On the other hand, these investigations have also revealed large variations in the depth to the water level at different locations within the study area, as well as a different response to precipitation events. Therefore, the interpolation of such data is likely to provide a skewed picture of the subsurface conditions, especially regarding the groundwater flow.

Textural properties of the soils (e.g., clay content, grain size and interconnection of the pore space) play an important role in the hydraulic conductivity of the subsurface materials, and thus in the ability of the soils to permit infiltration and groundwater flow. An increase in the clay content commonly reduces the effective porosity, and thus the hydraulic conductivity (K). Although analysis of sediments provides a direct measure of the textural properties, it fails to recover the spatial variability of the subsurface properties away from the drilling point and may provide little evidence regarding pore-space geometry. Geophysical methods have demonstrated the ability to gain information on subsurface properties with high spatial and temporal resolution in a non-invasive manner. In particular, electrical and electromagnetic methods sensing variations in the electrical conductivity of soils and rocks have been developed to evaluate changes in hydraulic properties (e.g., Danielsen et al., 2003; Linde et al., 2006; Slater, 2007; Binley et al., 2005; 2015; 2016). The link between electrical and hydraulic conductivity has also been previously addressed in landslide investigations through electrical resistivity monitoring (Supper et al., 2014; Travelletti et al., 2012; Perrone et al., 2014; Gance et al., 2016), yet excluding the contribution of surface conductivity to the bulk conductivity. Weller et al (2015) recently proposed a model linking the hydraulic conductivity and the polarization effect resolved for measurements collected at 1 Hz over a broad range of samples in the laboratory, considering both consolidated and unconsolidated rocks. Binley et al. (2016) revealed the applicability of such model to interpret time-domain induced polarization (TDIP) data collected at the field scale.

At the laboratory-scale, induced polarization (IP) measurements collected at different frequencies, the so-called spectral IP (SIP) method, have evidenced that textural properties controlling water flow also control the frequency-dependence of the complex conductivity. Accordingly, petrophysical models have been proposed to link the SIP response and the hydraulic conductivity (e.g., Slater, 2007; Revil and Florsch, 2010; Revil, 2013; Binley et al., 2015, Abdulsamad et al., 2019; Revil et al., 2020, and references therein). However, for landslide investigations, geophysical methods have been mainly used to map the geometry of the sliding plane (Bichler et al., 2004; Lapenna et al., 2003; 2005; Chambers et al., 2011) and monitor the landslide activity (see for example Whiteley et al., 2019 for a review). To the best of our knowledge, few studies have applied the IP method for understanding landslides (e.g., Marescot et al., 2008; Flores Orozco et al., 2018a; Gallistl et al., 2018). Gallistl et al. (2018) demonstrated that IP images permit a better mapping of structures favoring water flow or water storage in a shallow clay-rich landslide. Likewise, Flores Orozco et al. (2018a) revealed that IP images permit an improved delineation of the sliding plane geometry compared to investigations using solely resistivity results for the La Valette landslide. Moreover, the authors revealed that active areas of the landslide were in agreement with polarizable anomalies and a significant frequency-dependence; thus, suggesting a link between the pore-space geometries and the activity of the landslide. Nonetheless, Gallistl et al. (2018) as well as Flores Orozco et al. (2018a) evidenced the challenges to collect good quality IP data above 1 Hz due to electromagnetic coupling (EM-coupling). Recently, Flores Orozco et al. (2021) and Maierhofer et al. (2022) have demonstrated the possibility to minimize EM-coupling and improve the quality in IP readings up to 75 Hz through the use of coaxial cables.

Revil et al. (2020) proposed an approach to estimate the hydraulic conductivity and water content in an imaging framework through TDIP measurements. To properly account for the petrophysical model linking IP and hydraulic properties (see Revil, 2013), the authors invert for the parameters describing the frequency dependene of the electrical properties (e.g., normalized chargeability) directly from the voltage reading during current injection and after the current is switched off through the modeling of the primary and secondary current. While Abdulsamad et al. (2019) already demonstrated the applicability of TDIP for the hydraulic investigations of embankments; Revil et al. (2020) reveal the potential of the IP methods for landslide investigations beyond the delineation of the geometry of the sliding plane, and the quantitative interpretation of geophysical measurements at the field scale.

Revil et al. (2020) argue that the normalized chargeability, as obtained from the inversion of field-scale TDIP measurements, is consistent to the one obtained from the analysis of the frequency-dependence of IP measurements collected in the frequency-domain (FDIP). Hence, the authors obtain hydraulic conductivity and volumetric water content from TDIP, with their results supported through laboratory measurements. Accordingly, hydrogeological investigations can be conducted through TDIP measurements without the necessity to repeat data collection at different frequencies or by recording the full-waveform. However, the influences of the pulse length used to collect the decay-curve in the polarization data is not addressed by Revil et al. (2020), and only a qualitative analysis of the data-error is presented, although those two issues are critical for the application of the IP method for landslide investigations. On the one hand, short pulse lengths reduce the total acquisition time, but may not be able to capture the slow polarization responses. On the other hand, not all instruments permit to capture the entire decay curve, especially at the early times; thus, limiting the content of the IP data colleted with short pulse lengths. Hence, the selection of an adequate pulse plays a critical role in the quantitative estimation of IP parameters. Additionally, low polarization signatures, may result in readings distorted by noise due to poor signal-to-noise ratios (S/N), which in turn reduce the accuracy of the inversion results (e.g., Flores Orozco et al., 2012a; 2018a; 2018b and references therein).

In this study, we present TDIP and FDIP data collected at the Hofermuehle catchment in an area that is recently stable, but was active in the past and may reactivate in the future. Based on our measurements, we address in detail the advantages and drawbacks of both TDIP and FDIP techniques, in particular regarding the estimation of hydraulic properties. In particular, we aim at investigating the potential of IP data (single and multi-frequency) to identify clay rich areas with a poor drainage, and thus susceptible to sliding. To evaluate the frequency-dependence of the IP field data and subsurface electrical properties, we present the intrinsic response as measured in the laboratory for different samples retrieved from the site. We also compare field-scale K-estimations based on TDIP measurements, data collected at single frequency (with FDIP) and the analysis of multi-frequency IP data (i.e., SIP).

Additionally, we present independent estimations of the hydraulic conductivity based on a novel approach by Steiner et al. (2022) that permits the joint inversion of electrical resistivity tomography (ERT) and seismic refraction tomography (SRT) data sets taking into account the contribution of surface conductivity. Such inversion approach permits to solve for the spatial variations of the porosity in the imaging plane, which can then be used to independently solve for K. Accordingly, we can evaluate our hydraulic conductivity estimations from IP data through those obtained by means of the joint inversion.

Our results demonstrate that IP imaging results can map areas with poor drainage prone to land sliding. We also show that TDIP and single frequency FDIP provide very consistent results, yet a better understanding of the hydrogeological units may be resolved only by the analysis of the frequency-dependence through SIP measurements.

2. Material and methods

2.1. The complex conductivity as an expression of the electrical conductivity and polarization properties of the subsurface

The IP method is a geophysical electrical technique based on four-electrode measurements, where one electrode pair is used to measure the electrical impedance (i.e., complex-valued voltages) resulting from the injection of current in a second electrode pair. For a complete revision of the method we refer to other works (Binley and Kemna, 2005; Binley and Slater, 2020). Imaging measurements consist of hundreds to thousands of four-electrode readings collected with tens to hundreds of electrodes placed along profiles (2D) or planes (3D). The inversion of such imaging datasets permits solving for the variations of the complex resistivity (CR) – or its inverse the complex conductivity (CC). Hence, this method is also known as CR or CC imaging or electrical impedance tomography (EIT). The complex-valued electrical conductivity (σ^*), expressed in terms of its real (σ') and imaginary (σ'') components, permits the representation of both the electrical conductive and capacitive properties of the materials. Alternatively, the CC can also be expressed in terms of its magnitude ($|\sigma|$) and phase angle (φ), such as:

$$\sigma^* = \sigma' + i\sigma'' = |\sigma| e^{i\varphi} \tag{1}$$

Considering that the polarization response of natural media without electrical conductors is commonly low (<100 mrads), it can be assumed that $\sigma' = |\sigma|$ and that the phase angle is given by the ratio of polarization to conduction ($\varphi \approx \sigma''/\sigma'$).

The electrical conductivity represents the ability of materials to permit the migration of ions, which in case of natural media with a negligible amount of electronic conductors (i.e., metals), takes place along two paths: through the electrolyte and within the electrical double layer (EDL) formed at the contact between grain and the electrolyte. On the one hand, the electrolytic conduction (σ_{el}) is defined by the water saturation (S_w), the porosity (Φ) and the fluid conductivity (σ_f) (e.g., the electrical conductivity of the groundwater). On the other hand, grains with a high surface charge, such as clays, attract charges from the electrolyte forming an EDL, which also permits the conduction of current by surface conductivity (σ_s'). Additionally, the charges accumulated at the EDL polarize in the direction of the injected current, which contributes to the imaginary component of the complex conductivity (σ_s''). The strength of such polarization is primarily controlled by the surface charge and surface area of the grain (for further details we recommend Lesmes and Friedman, 2005; Slater and Glaser, 2003; Binley and Slater, 2020). Thus, at low frequencies (<1 kHz), the complex conductivity of the subsurface can be written as:

$$\sigma^*(\omega) = \sigma'(\omega) + i\sigma''(\omega) = \sigma_{el} + i\sigma_s^*(\omega) = [S_w^n \Phi^m \sigma_f + \sigma_s'(\omega)] + i\sigma_s''(\omega) \tag{2}$$

In Eq. (2), σ_s^* represents the complex-valued surface conductivity, $i = \sqrt{-1}$ the imaginary unit, ω the angular frequency related to the frequency f ($\omega = 2\pi f$) of the alternating current injected to the ground and n is the so-called saturation exponent associated to changes in the electrical conductivity from partially to fully saturated rocks (see Glover, 2017 and references therein). The cementation exponent m is related to the connectivity of the pores permitting groundwater flow (Archie, 1942; Sen et al., 1981). Accordingly, the formation factor F (dimensionless), linking the amount of pore volume (i.e., porosity) and the way such pores are arranged (for a review we refer to Glover, 2009), can be written as:

$$F = \Phi^{-m} \tag{3}$$

As observed in Eq. (2), the electrical conductivity is controlled by both σ_{el} and the frequency-dependent σ_s', while the capacitive properties, or polarization, are only controlled by the surface conductivity (σ_s'').

Measurements collected at different frequencies (below ~ 1 kHz) can be used to gain information about the frequency-dependence of the complex conductivity in the so-called spectral IP (SIP) or multi-frequency IP. Plenty of studies have demonstrated a link between the SIP response and textural and hydraulic properties of soils (e.g., Binley et al., 2005; Zisser et al., 2010; Revil, 2013; and references therein). The Cole-Cole model has been widely adopted to describe the frequency-dependence of the complex conductivity, which can be written in terms of the electrical conductivity (e.g., see Tarasov and Titov, 2013) as:

$$\sigma^*(\omega) = \sigma_\infty \left(1 - \frac{M}{1 + (i\omega\tau)^c}\right) \tag{4}$$

In Eq. (4), M is the chargeability, which is defined in terms of the conductivity at high and low frequencies (σ_∞ and σ_0 respectively) as $M = (\sigma_\infty - \sigma_0)/\sigma_\infty$, while τ is the relaxation time (in s), inversely proportional to the critical frequency (f_c, with $f_c = 1/2\pi\tau$), which refers to the frequency at which the highest polarization response is observed (for further details see Tarasov and Titov, 2013). The exponent c (dimensionless) describes the broadness of the frequency-dependence. The strength of the polarization (e.g., Lesmes and Frye, 2001) is quantified by the normalized chargeability (in S/m), defined by:

$$M_n = M\sigma_\infty = \sigma_\infty - \sigma_0 \tag{5}$$

2.2. Hydraulic conductivity (K) estimations based on IP measurements

In the last decade several approaches have been proposed to estimate the hydraulic conductivity K (or expressed in terms of the hydraulic permeability, k) from IP measurements (e.g., Hördt et al., 2007; Slater, 2007; Revil and Florsch, 2010; Kemna et al., 2012; Weller et al., 2015). Börner et al. (1996) proposed an inverse correlation between hydraulic conductivity and the induced polarization (e.g., $K \approx (F\sigma'')^{-1}$) assuming that σ'' is a direct measure of the surface area per unit pore volume (S_{por}), the inverse of the hydraulic radius (see Slater, 2007 and references therein). Kemna et al. (2004) applied the model proposed by Börner et al. (1996) to obtain k estimations from cross-borehole TDIP imaging data. Slater and Lesmes (2002) extended the Börner et al. (1996) model to fit a wide range of samples from unconsolidated sediments. However, in their study the authors only investigated samples with a limited range in porosities (Slater, 2007). More recently, Weller et al. (2015) demonstrated the possibility to predict the hydraulic permeability by means of IP measurements collected at 1 Hz over a large number of samples considering both unconsolidated sediments and sandstones. In terms of hydraulic conductivity such model can be written as:

$$K = \frac{g\delta}{\mu} \frac{3.47x10^{-16}\sigma_0^{1.11}}{\sigma''^{2.41}} \tag{6}$$

Moreover, Weller et al. (2015) demonstrated that a slightly better prediction can be obtained when using the normalized chargeability, with such model written in terms of the hydraulic conductivity as:

$$K = \frac{g\delta}{\mu} \frac{4.03x10^{-9}}{F^{3.68} M_n^{1.19}} \tag{7}$$

In our study, we use reference values for groundwater dynamic viscosity ($\mu = 1.0016 \times 10$ kg m^{-1} s^{-1}) and density ($\delta = 1000$ kg m^{-3}), as well as for gravitational acceleration (g), which we assumed to be 9.81 m s^{-2}.

Alternatively, Revil et al. (2020) apply a different set of equations to derive the volumetric water content (Θ) and the hydraulic conductivity from TDIP data sets. Such petrophysical model is based on the dynamic Stern layer model (after Revil et al., 2017). Written in terms of Θ, the cation exchange capacity (CEC) and the density of the grains (δ_g), the dynamic Stern layer model can be written (Revil, 2013; Revil et al., 2020) as:

$$\sigma_0 = \Theta^m \sigma_f + \Theta^{m-1} \delta_g \beta CEC \tag{8}$$

$$\sigma_\infty = \Theta^m \sigma_f + \Theta^{m-1} \delta_g (\beta - \lambda) CEC \quad (9)$$

$$M_n = \Theta^{m-1} \delta_g \lambda CEC \quad (10)$$

In Eqs. (8)–(10), β denotes the apparent mobility of counterions for surface conduction and λ the apparent mobility of the counterions for the polarization associated with the quadrature conductivity (Revil et al., 2017). Abdulsamad et al. (2019) argue that Eqs. (8)–(10) can be applied for the quantitative interpretation of TDIP in terms of the hydraulic permeability, considering that M_n and σ_0 are obtained through the inversion of the data. Written in terms of the hydraulic conductivity, the model proposed by Abdulsamad et al. (2019) is given by:

$$K \approx \frac{g\delta}{\mu} \frac{k_0 \Theta^6}{(\delta_g CEC)^2} \quad (11)$$

In Eq. (11), $k_0 = 10^{4.3}$ (dimensionless) and the variables CEC and Θ can be derived from combinations of Eqs. (8) and (10). In particular, as presented in Revil et al. (2020) the volumetric water content is obtained by:

$$\Theta = \left[\frac{1}{\sigma_f} \left(\sigma_\infty - \frac{M_n}{R} \right) \right]^{\frac{1}{m}} \quad (12)$$

with $R = \frac{\lambda}{\beta} \approx 0.1 \pm 0.02$ after Revil et al. (2020).

2.3. Time-domain and frequency-domain IP measurements at the Hofermuehle site

Investigations presented here were conducted in pasture lands located to the East of the most active area of the Hofermuehle site, which has been stable over the last 10 years and is defined as a dormant landslide. Fig. 1 shows the area under investigation as well as existing ground truth information at the study site. Measurements in time-domain (TDIP) were collected in November 2017 using a Syscal pro 72 switch unit (from IRIS instruments), which permits connecting 72 electrodes and collecting ten voltage readings simultaneously for a given current injection using ten measuring channels. In TDIP, the voltage is measured during the current injection to compute the transfer resistance. Subsequent voltage readings are collected once the current is switched off to calculate the integral chargeability (M_{int}), which is a measure of the polarization effect. TDIP measurements presented here were conducted along six parallel lines roughly oriented North-South with 36 electrodes (in each line) with a separation of 5 m between electrodes and profiles as presented in Fig. 1. Measurements along line L1 were conducted with different pulse lengths, namely 0.25, 0.5, 1, 2 and 4 seconds (s) to investigate their influence in the M_{int} readings, with

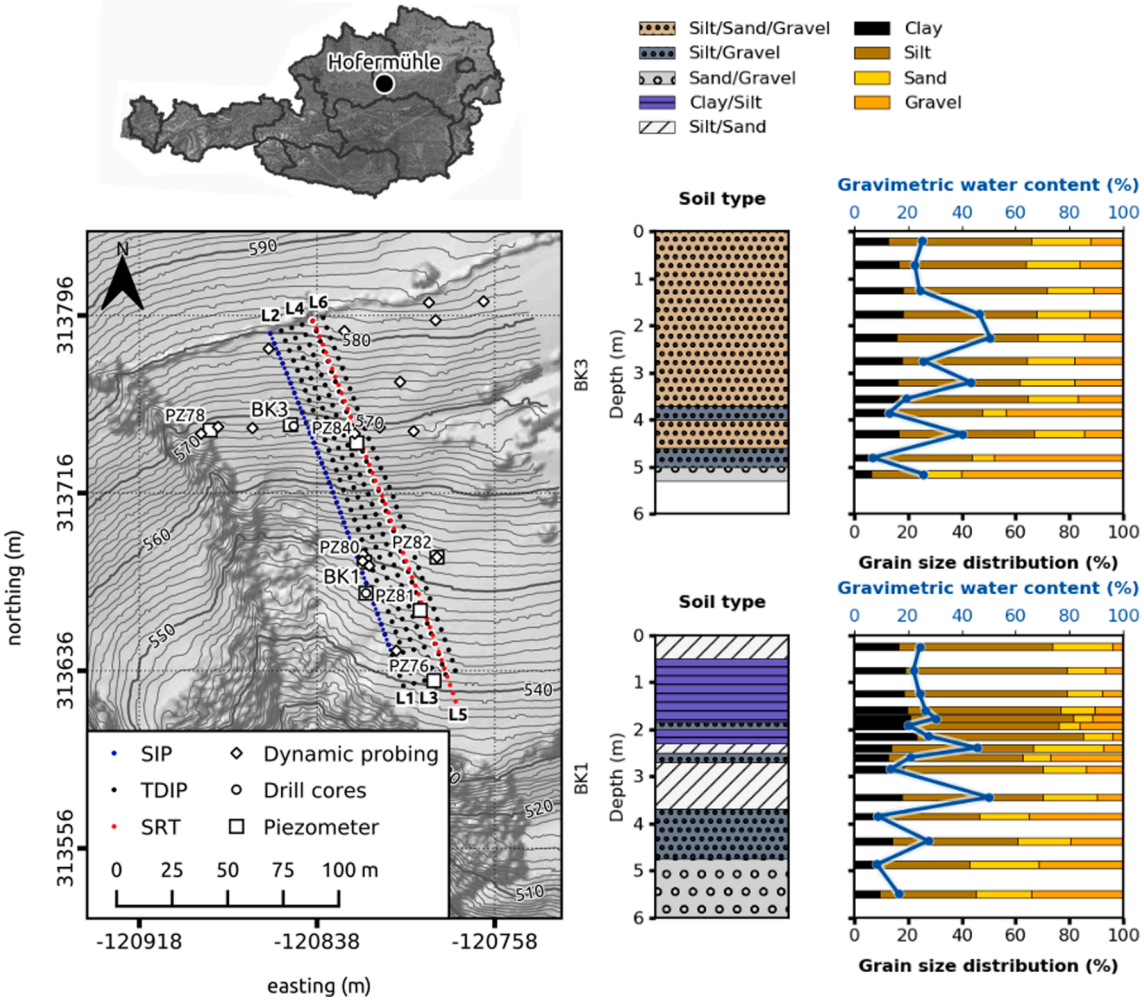

Fig. 1. Location and existing ground truth information at the Hofermuehle landslide located in Austria. The map presents the elevation of the study area and the position of the available ground truth data as well as the location of the geophysical lines. The analysis of samples collected from the cores BK1 and BK3 are used to construct the plots illustrating the lithological logs (using the DIN18196 classification), grain size analysis and variations in gravimetric water content. The position of the electrodes for the collection of time- and frequency-domain induced polarization (TDIP and FDIP) is indicated with the black and blue symbols respectively, whereas the position of the geophones for the seismic refraction tomography (SRT) is indicated with the red ones.

samplings of the decay curve favoring slow polarization effects for long pulse lengths. We collected lines L2 to L6 with a pulse length of 500 ms, which revealed the best compromise between short acquisition time and high S/N, as well as the possibility to sample the decay curve with the maximum of 20 windows available in the Syscal pro unit. We used a dipole–dipole (DD) skip-3 configuration, which means that current injection and voltage measurements are conducted with electrode pairs skipping three electrodes within them. Three electrodes were the minimum separation between the current and potential dipole in this configuration; whereas the maximum separation was 26 electrodes to use the 10 measuring channels. To increase the resolution in the near surface, we also include DD skip-0, skip-1 and skip-2 readings, always considering a maximum spread defined by the 10 measuring channels and a minimum separation between current and potential dipoles defined by the skip. Reciprocals are available only for readings along line L1 collected with 500 ms pulse length, with reciprocal readings referring to those collected after interchanging the electrodes used for current and potential dipoles (e.g., Flores Orozco et al., 2018a). Table 1 summarizes the settings for collecting the different TDIP data.

Frequency-domain (FDIP) measurements were collected in September 2021 along line L1 using a Data Acquisition System Multi-source (DASM, from MPT-IRIS Inc.), deploying 64 electrodes with a separation of 2.5 m between them. Such instrument allows to physically separate the transmitter (i.e., current injections) and the receiver (used for voltage readings); thus, minimizing the contamination of the data due to parasitic electromagnetic (EM) fields arising from cross talking within the device (see Flores Orozco et al., 2018b; 2021). As the transmitter and receiver are separated, in a first step we collected measurements connecting the transmitter to odd number electrodes, while electrodes with even numbers were connected to the receiver. In a second step, we interchanged the position of the transmitter and receiver to permit the collection of all possible combinations. In case of FDIP, the device records the electrical impedance given by the voltage to current ratio (impedance magnitude or transfer resistances) and the phase-shift between the sinusoidal current and voltage. Measurements were recollected for each quadrupole across 16 frequencies distributed in the range between 0.25 and 240 Hz to gain information about the frequency-dependence of the IP data (i.e., the complex conductivity). Measurements with the DASM were conducted using a DD skip-3 to permit comparison with the TDIP readings with a maximum separation of 16 electrodes between current and potential dipoles. We also collected a DD skip-1 configuration with all possible combinations, including the maximum separation between current and potential dipoles (i.e., 60 electrodes). The use of separated cables, as deployed here, does not permit to collect DD data with an even number of skipped electrodes. All FDIP data sets presented here were collected as normal-reciprocal pairs.

Both time-domain and frequency-domain measurements were conducted with multicore cables, although Flores Orozco et al. (2021) revealed that such cables cause distortions in the measurements of the impedance phase-shift due to cross talking between the cables. Nonetheless, the same study demonstrated that such EM fields minimally distort TDIP readings, as the M_{int} is only measured after the current injection is switched off. In case of FDIP measurements, the separation of transmitter and receiver as well as cables connected to current and voltage electrodes also minimize cross talking (i.e., Flores Orozco et al., 2021; Dahlin and Leroux, 2012). Inductive EM coupling with the subsurface materials is known to be proportional to the conductivity of the subsurface, the acquisition frequency and the square of the length of the cables (Hallof, 1974). Therefore, EM coupling in the FDIP is expected for high frequencies and in our data we only observed a linear increase in the IP data with increasing the frequencies above 70 Hz, evidencing possible EM-coupling at such frequencies. Such data contamination may not be observed in TDIP considering the 10 Hz analogous filter in the Syscal unit (see Martin et al., 2020).

2.4. Analysis in soil samples: Grain size analysis and SIP measurements

We conducted multi-frequency FDIP measurements (i.e., SIP) in soil samples recovered from two wells to evaluate the frequency-dependence of the IP data observed at the field scale. The SIP measurements in the lab were conducted in 19 samples, 11 taken from BK1 (extracted from depths between 0.25 m and 5.5 m), and 8 samples from BK3 (extracted in depths between 0.25 m and 6 m). The grain size distribution in the soil samples investigated here is illustrated in Fig. 1, together with the lithological logs constructed using the soil classification DIN 18196. Complementary information here corresponds to four dynamic probing heavy (DPH) and groundwater levels measured in piezometers as shown in Fig. 1. Details on the grain size analysis and DPH can be found in Stumvoll et al., (2022).

For the collection of SIP data in the soil samples, we used the PSIP (portable spectral induced polarization) unit (from Ontash & Ermac Inc.), which is an instrument with high accuracy commonly used for laboratory investigations (e.g., Mellage et al., 2018). The sample holder is a cylindrical probe made of PVC with an internal diameter of 40 mm and a length of 150 mm. Current electrodes are located at each end of the probe and consist of a mesh of stainless steel covering the entire cross-sectional area of the holder. For the voltage measurements, the electrodes are placed with a separation of 50 mm between each other and to the current electrodes. Considering the 4-measuring channels available in the PSIP unit, the sample holder is designed to collect simultaneously three voltage readings, with each pair of electrodes placed around the column with a distance of 41.9 mm among them. Accordingly, one measurement represents the average of three electrical impedance measurements (one for each voltage pair) in the frequency range between 0.01 Hz and 10 kHz, consisting of 61 frequencies, with ten frequencies in each logarithm decade linearly distributed. The potential electrodes are made of stainless steel and drilled 1–2 mm deep

Table 1
Acquisition settings for time-domain induced polarization (TDIP) collected along lines 1 to 6. For completeness we provide the acquisition frequencies for the frequency-domain induced polarization (FDIP) data collected along line 1. The IP gates refer to the number of sampling points used to collect the integral chargeability within the sampling time after switching the current off (plus the delay). The DD-skip refers to the dipole length used for the data collection, with the acquisition times refer to the total time needed to collect the entire imaging data set.

Data	Line	Pulse length (ms)	Delay (ms)	IP gates	Sampling time (ms)	DD-skip	Levels	Acquisition time (minutes)	Electrodes and spacing
TDIP	1	250	20	7	140	0, 1, 2, 3, 4	10	7	36 – 5m
TDIP	1	500	20	20	400	0, 1, 2, 3, 4	10	11	36 – 5m
TDIP	1	1000	40	20	880	0, 1, 2, 3, 4	10	19	36 – 5m
TDIP	1	2000	40	20	1800	0, 1, 2, 3, 4	10	35	36 – 5m
TDIP	1	4000	160	20	3520	0, 1, 2, 3, 4	10	66	36 – 5m
TDIP	2	500	20	20	400	0, 1, 2, 3, 4	10	11	36 – 5m
TDIP	3	500	20	20	400	0, 1, 2, 3, 4	10	11	36 – 5m
TDIP	4	500	20	20	400	0, 1, 2, 3, 4	10	11	36 – 5m
TDIP	5	500	20	20	400	0, 1, 2, 3, 4	10	11	36 – 5m
TDIP	6	500	20	20	400	0, 1, 2, 3, 4	10	11	36 – 5m
FDIP	1	0.5, 1, 3, 6, 8, 10, 15, 25, 37.5, 60, 75, 92, 120, 130, 171, 240 (Hz)				1, 3	16	194	64 – 2.5m

into the sample through the cylindrical barrel yet these are not in direct contact with the soil within the sample holder, following a similar setup as presented by Cassiani et al. (2009). We used demineralized water to saturate the samples and a wet packing, where the column was filled by adding soil samples and water simultaneously to avoid the formation of bubbles, which decrease the quality of the readings. Measurements were collected 1 and 24 h after the packing to investigate changes in the signal due to lack of equilibrium (e.g., Ustra et al., 2012). As we observed minimal changes we only present the data collected 24 h after the packing. The geometric factor was estimated using the approach presented in López-Sánchez and Mansilla-Plaza (2017) and experimentally. For the latter case, we filled the column with tap water, with the geometric factor obtained as the ratio of the fluid conductivity of the tap water divided by the resistance measured. We observed negligible variations in the geometric factor obtained (numerically and experimentally) for our three voltage dipoles, as well as impedance phase values close to zero mrads (as expected) with fluctuations of ±0.15 mrads in the range between 1 mHz and 100 Hz. For the sample holder only filled with water, we observed an increase in the phase readings with increasing the frequency due to EM coupling, yet values still below 5 mrads at 1 kHz, demonstrating the good quality of our data and the experimental set-up.

Similar to previous studies (e.g., Revil, 2012; Weller et al., 2015; Revil et al., 2017), we conducted SIP measurements in four soil samples, with measurements repeated in each sample after varying the salinity to estimate the formation factor F. The preparation and packing of the sample into the column followed the recommendations by Bairlein et al. (2014). Before the measurements at each salinity, the soil samples are first dried, then mixed with a brine at a given salinity and packed into the sample holder to collect the SIP data. Such steps are repeated for brines at different salinity. For the estimation of F and m, it is assumed that $\sigma_s^{'}$ is salinity-independent and a linear relationship between σ' and σ_f exists, such as:

$$\sigma^{'} = \frac{1}{F}\sigma_f + \sigma_s^{'} \tag{13}$$

These measurements were conducted in a similar probe as the one described by Bairlein et al. (2014), with a cell diameter of 2.5 cm and a total length of 16.6 cm. The soil samples were saturated with three to four different sodium chloride brines (with σ_f ranging from 0.5 to 140 mS/m) as well as demineralized water as reference. The porosity of the samples was estimated based on the volume of the sample holder and the difference between the saturated and dry sample mass. Combination of Eqs. (3) and (13) were used to determine the cementation exponent.

2.5. Complementary data: field-scale seismic refraction tomography (SRT)

We also conducted a seismic survey to (1) validate the interpretation of the IP imaging results regarding the geometry of layers of potential instability, i.e., the potential shear surface, and (2) solve directly for the porosity (Φ), saturation (S_w) through the joint inversion of electrical resistivity and seismic refraction data as presented recently by Steiner et al. (2022). The TDIP readings revealed minimal lateral variations in the electrical response, hence we maintained a distance of several meters between the SRT and FDIP profiles to allow for the simultaneous collection of these data sets and avoid a possible contamination between the readings. The seismic refraction data were measured using a Summit data acquisition system (from DMT) with a recording length of 1024 ms, a sampling rate of 0.25 ms, and a pre-trigger of 20 ms. We deployed 48 geophones (corner frequency 30 Hz) at the ground surface with 4 m spacing between them. At each geophone position, we generated seismic waves by striking a plastic plate (3.5 cm thick) with a 7.5 kg sledge-hammer and stacked four hammer blows to ensure an adequate S/N ratio.

2.6. Processing and inversion of TDIP, FDIP, SRT data

For FDIP measurements, we filtered all readings whose normal-reciprocal misfit (NRM) was larger than the standard deviations of the NRM of the entire data set. This was done for data sets collected at each frequency (see Flores Orozco et al., 2012a; 2018b). In a second step, we compared the data sets collected at the 16 frequencies and kept only those quadrupoles found in all data sets. The TDIP data sets were processed using the decay-curve analysis proposed by Flores Orozco et al. (2018a). Integral chargeability readings from TDIP were linearly converted to impedance phase values to permit the inversion in terms of complex resistivity. Such approach has been demonstrated to permit a quantitative comparison of the data (Flores Orozco et al., 2012a), although it assumes a constant phase value, i.e., neglects the frequency-dependence in the data. Such assumption is valid considering the relatively short time range used to sample the decay curve. Accordingly, the conversion factor needs to be recalculated for data collected with different pulse lengths.

We used CRTomo (Kemna, 2000), a smoothness-constrained algorithm based on a complex calculus, to invert electrical impedances collected at a given frequency and solve for the distribution of the complex resistivity as a 2D section. The algorithm allows fitting the data to a level of confidence as defined by a data-error parameter to minimize the risk of creating artifacts within the inversion (Flores Orozco et al., 2012b); further details about the inversion algorithm can be found in Kemna (2000). Error parameters were defined as 1 % and 0.1 mΩ for the inversion, yet a robust inversion scheme was deployed. All inversion results presented here converged to an error-weighted root-mean-square (RMS) error of ca. 1.0, which indicates that the forward response of the inverted complex conductivity models accurately resolved for the data accounting for the data-error. For the 3D inversion of IP data we used ResIPy (Blanchy et al., 2020), which is also based on complex calculus and the fitting of the data to a defined error-model (see Binley and Kemna, 2005).

To gain information about the frequency-dependence of the σ^*, we fitted a Cole-Cole model (Eq. (4)) pixel-wise to the complex conductivity imaging results obtained after the inversion of the FDIP data sets. We used the algorithm by Weigand and Kemna (2016) to fit the Cole-Cole models, with the root-mean-square error (RSME) computed as the misfit between the data and the fitted model. Initial analysis of the results demonstrated a first peak below 60 Hz and the increase in the phase values for higher frequencies. Accordingly, in this study we only present the Cole-Cole parameters obtained for fitting the imaging results obtained between 1 and 60 Hz, to avoid the interpretation of possible EM-coupling (Pelton et al., 1978; Flores Orozco et al., 2013; 2018a,b; 2021) or Maxwell-Wagner polarization (e.g., Revil, 2013) effects in the data.

From the seismic waveform data, we manually determined the P-wave travel time for each shot-geophone pair in an iterative process based on different data gathered, i.e., common shot, common receiver and common offset. We applied a 100 Hz low-pass filter on the data to enhance the perceptibility of the P-wave arrivals. Such filter mitigates the influence of high frequency noise, which is particularly relevant for larger offsets, i.e., larger distances between shot and geophone. For the joint inversion of SRT and resistivity tomography data, we used the petrophysical joint inversion framework implemented by Wagner et al. (2019) built upon the forward modelling and inversion capabilities provided by the open-source library pyGIMLi (Rücker et al., 2017). In particular, this joint inversion scheme solves for the volumetric water, air, ice and rock content, yet the underlying petrophysical model does not account for the surface conduction. Recent investigations (Mollaret et al., 2020; Steiner et al., 2021) have demonstrated the applicability of this petrophysical joint inversion scheme for field data collected at different alpine sites. Exploiting the frequency-dependence of σ_s, Steiner et al. (2022) proposed an extension to the petrophysical joint inversion algorithm that simultaneously inverts seismic travel times as well as electrical resistivity measurements collected at two frequencies (i.e., at

low and high frequency) to quantify the surface conductivity during the parameter estimation. Built upon the formulations of the mechanistic polarization model by Revil (2013), as presented in Eqs. (8)–(10) above, the modified joint inversion scheme solves for the volumetric water, air and rock content, while the surface conductivity is quantified by means of the CEC. For more details about the joint inversion schema including surface conduction we refer to Steiner et al. (2022).

In this study, we used the transfer resistances recorded during FDIP measurements collected at 1 and 60 Hz to be consistent with the above mentioned Cole-Cole analysis. In the petrophysical model underlying the joint inversion framework we set the parameters m and n (see Eq. (2)) as 2 and 1.5 respectively; whereas the conductivity of the groundwater 0.075 mS/m as measured at the site. With regard to the mechanical properties, we set seismic P-wave velocities (V_p) of water, air and rock as 1500 m/s, 330 m/s and 3500 m/s, and the density of the silty loam in the Hofermuehle site is assumed to be 1300 kg m^{-3}. For the inversion we used an initial homogeneous porosity model of 40 % to honor the porosity measured in the soil samples. No changes were observed if the initial porosity model was defined as a gradient with increasing values at depth. Joint inversion results presented here converged to an error-weighted root-mean-square (RMS) error close to 1.5, which indicates that the resolved subsurface model sufficiently explains the measured data within their respective error bounds.

3. Results

3.1. Time-domain IP surveys: The effect of the pulse length and a first map of the study area

In Fig. 2, we present the visualization of the TDIP data collected along line L1 with different pulse lengths. The data are presented in terms of the apparent resistivity (ρ_{app}) and integral chargeability (M_{int}). The ρ_{app} refers to the multiplication of the measured transfer resistances by the geometric factor, which in this case was modelled using CRTomo to account for the topography; whereas the M_{int} is directly obtained from the measurements without further conversions. The position of the pixel values representing the different measurements is based on the separation between the mid-point of the current and potential dipoles, allowing for the investigation of the variability in the measured data at different pulse lengths. The ρ_{app} plots reveal negligible changes between acquisitions using different pulse lengths, whereas large changes are observed in the M_{int}. In particular, for measurements along line L1, M_{int} readings with short pulse lengths are at least two times higher than those collected at 1000, 2000 and 4000 ms. We also observe that the pseudosections of M_{int} are smoother for short pulse lengths, while pulse lengths > 1000 ms show more abrupt changes between adjacent measurements, especially for deeper readings, as they are related to lower voltage readings (e.g., Flores Orozco et al., 2018a) and, thus, lower S/N.

Fig. 3 presents the imaging results for the TDIP data collected along lines L1 to L6 expressed in terms of the real and imaginary components

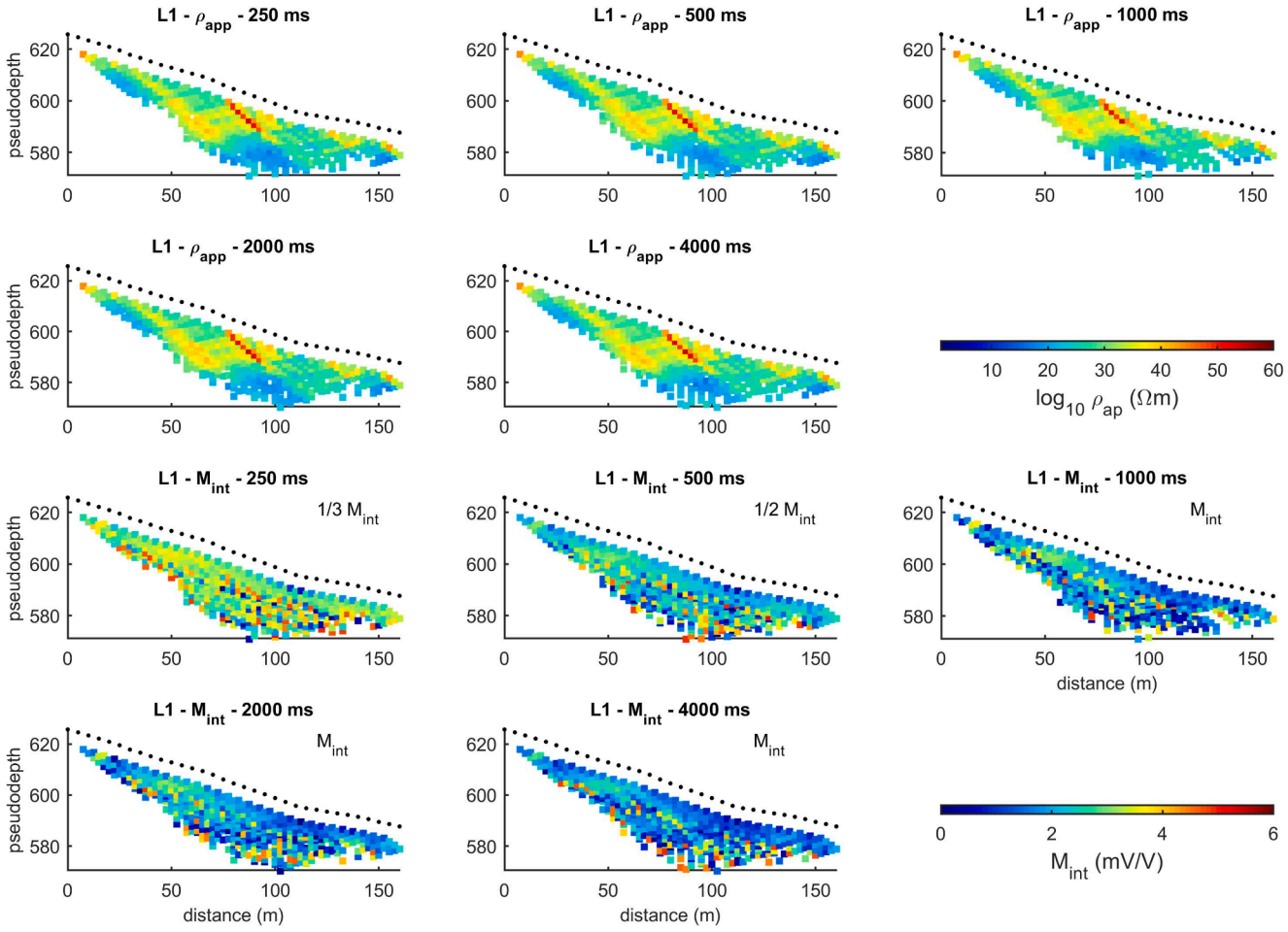

Fig. 2. Visualization of the TDIP raw data collected along line L1 with five different pulse lengths. The raw data are expressed in terms of the apparent resistivity (ρ_{app}) and the integral chargeability (M_{int}). The M_{int} readings collected at pulse lengths of 250 and 500 ms are scaled (1/3 and 1/2 respectively) to permit using the same color scale for all measurements. The black dots represent the position of the electrodes at the surface.

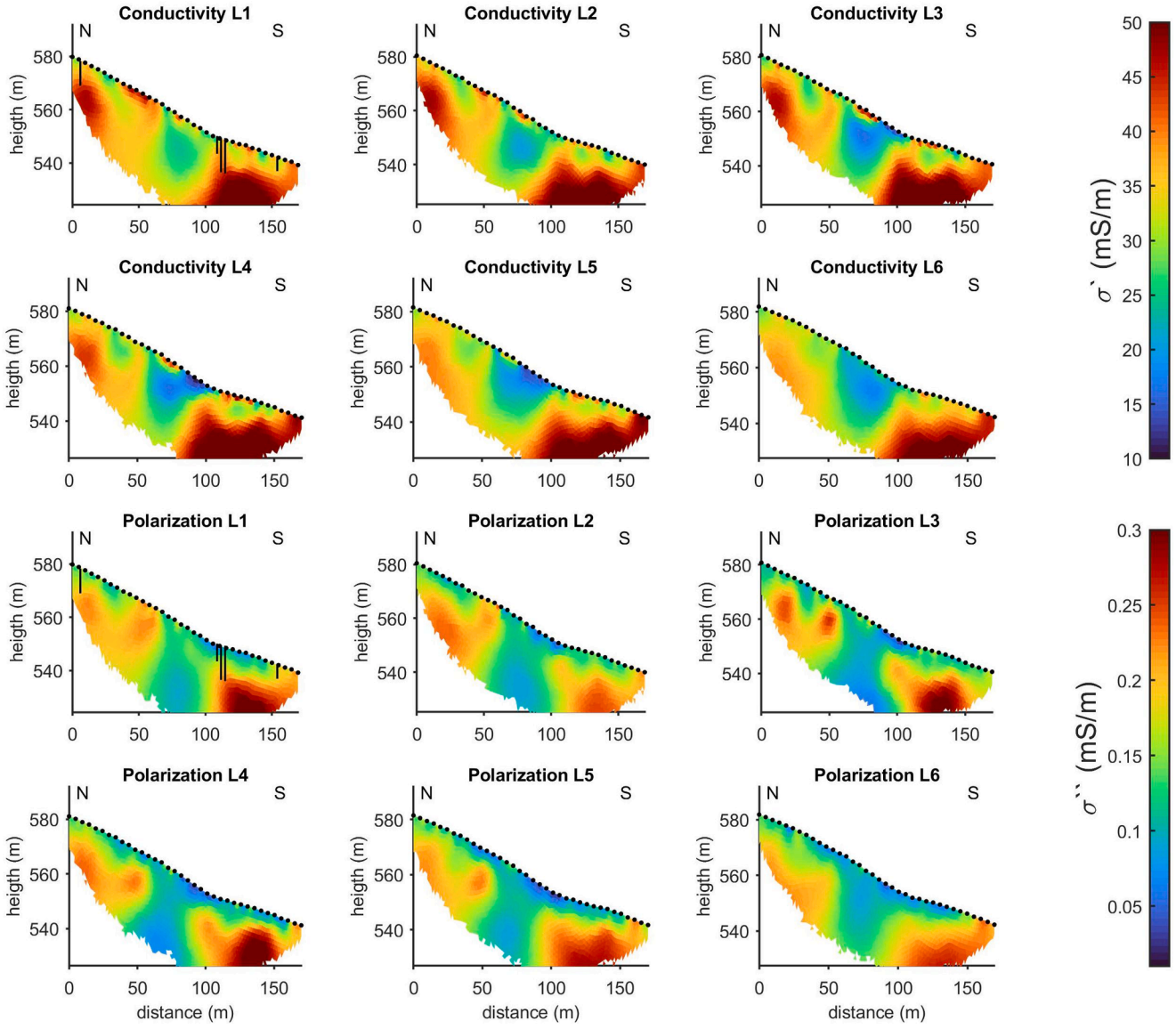

Fig. 3. Inversion results for TDIP mapping data expressed in terms of the real (σ') and imaginary (σ'') components of the complex conductivity from line L1 to L6. The black points in each image represent the electrodes at the surface. The vertical lines imposed in plots of L1 indicate the position and maximum depth reached with dynamic probing heavy (DPH). The plots have a vertical exaggeration 2:1 to better identify subsurface changes at depth.

of the complex conductivity. We resolved consistent images for all profiles, which suggest minimal lateral variations in East-West direction and significant changes can be observed in North-South direction. The DPH information available along the IP lines is indicated in the imaging results in Fig. 3 as vertical lines that extend to the depth of refusal interpreted as the contact with bedrock (see Stumvoll et al.,2022). As exhibited in Fig. 3, the bedrock resolved by means of the DPH is in agreement with the contact to the highest conductive ($\sigma' > 40$ mS/m) and polarizable ($\sigma'' > 0.2$ mS/m) materials resolved with the inversion of TDIP data. The DPH resolved a shallower contact to the bedrock at ca. 100 m (along profile distance), which is also consistent with a lateral change in the shape of the highest conductivity and polarization values. Groundwater levels are expected at ca. 1 m bgs along the TDIP lines with the only exception of the piezometer PZ-78 located at the end of the Line 1, which revealed a depth of ca 3 m (see Table 2). Both σ_{el} and σ_s^* are dependent on saturation; thus, unsaturated soils explain the low conductivity and polarization response in the top soils (within 1 to 3 m depth) and lateral changes indicating variations in the textural properties. Below the top soil layer, between ca. 3 and 10 m depth, the moderate σ' and σ'' values are related to weathered materials; whereas the high polarization and conductivity values in the bedrock correspond to materials of the Flysch formation. However, between 60 and 90 m along the profile there is a clear anomaly characterized by lowest σ' and

Table 2
Depth to the water table observed in 2021. The values represent the mean depth (below ground surface, bgs) from observations in 2021 for the piezometers in the experimental plot at the Hofermuehle landslide. We provide also the computed variance.

Piezometer	Water level (m bgs)	Variance (m)
BK1	0.72	0.01
BK3	0.67	0.068
PZ-76	1.27	0.016
PZ-78	3.07	0.008
PZ-80	1.06	0.048
PZ-81	1.09	0.053
PZ-82	0.69	0.052
PZ-84	3.03	0.058

σ'' values, suggesting a lower content of clay minerals than to both ends of the profile. Increasing σ^* values are related to increasing clay contents and the contribution of both electrolytic and surface conduction. The polarization of clay is expected to increase with frequency, with a maximum around 100 Hz (e.g., Leroy and Revil, 2009). However, the instrument deployed has a built-in analogue low pass filter, limiting the content of the data below the cut-off frequency of 10 Hz (Martin et al., 2020). The lack of information in M_{int} in the early times (i.e., above 10 Hz) explains the relatively low polarization values observed in Fig. 3. Such interpretation cannot be validated as the steep slope forbids the collection of soil samples or the conduction of DPH on top of the low polarization anomaly. Due to the low σ' and σ'' values these anomalies indicate areas characterized by coarse grain sizes (e.g., sands), thus facilitating infiltration (in the top soils) as well as groundwater drainage at depth.

TDIP anomalies characterized by high conductivity (>40 mS/m) also correspond with the highest polarization values (>0.2 mS/m); thus, likely indicate high clay content, i.e., grains characterized by high surface area and charge where both surface and electrolytic conduction contribute to the observed bulk conductivity. Increasing the clay content commonly reduces the hydraulic conductivity, and likely such polarizable structures hinder groundwater flow. Hence, the combined analysis of conductivity and polarization results may improve the interpretation of the electrical images and the delineation of subsurface structures controlling water flow. Nonetheless, the TDIP inversion results provide no information on the actual frequency-dependence of the complex conductivity and taking into account the limited bandwidth in the frequency content recored by the Syscal pro unit (Martin et al., 2020), we opted to present the σ^* images obtained from TDIP linearly converted at a frequency of 1 Hz.

3.2. Frequency-domain imaging results for data collected at line L1

The inversion of FDIP data resolved in general for negligible changes in the conductivity (σ') at different frequencies. In contrast, the polarization images reveal a considerable frequency-dependence, with the σ'' increasing over two orders of magnitude with increasing the frequency from 1 to 240 Hz. Hence, in Fig. 4 we present the conductivity imaging results for data collected at 1 Hz as well as the polarization images (σ'') resolved at different frequencies. Inversion results obtained at 1 Hz are of particular interest, as this is the frequency used in the petrophysical model proposed by Weller et al. (2015) to predict K from FDIP measurements. Due to the large differences in the range of values, we use different color scales to present FDIP and TDIP imaging results. Plots in Fig. 4 reveal that FDIP imaging results are not deep enough to capture the response from the bedrock, with the sensitivity of the data sets only recovering the response from the weathered materials. This is due to the combination of a shorter electrode spacing and profile length, as well as the EM coupling affecting the readings with a low S/N, i.e., those deep measurements related to large separation between current and potential dipoles.

As described above, the groundwater table is expected at 1 m bgs; thus explaining the low polarization and conductivity observed in the unsaturated soils at the top soil layer also in agreement with TDIP images presented before. The anomalous region between 60 and 90 m distance shows low polarization values across all frequencies under investigation; thus, supporting our interpretation of a low clay content, as proposed for the interpretation of TDIP results. Within the weathered materials, the main variations are observed at depths below ca. 5 m, where the polarization increases, especially for high frequencies. Fine grains are related to shorter times to fully establish the polarization of

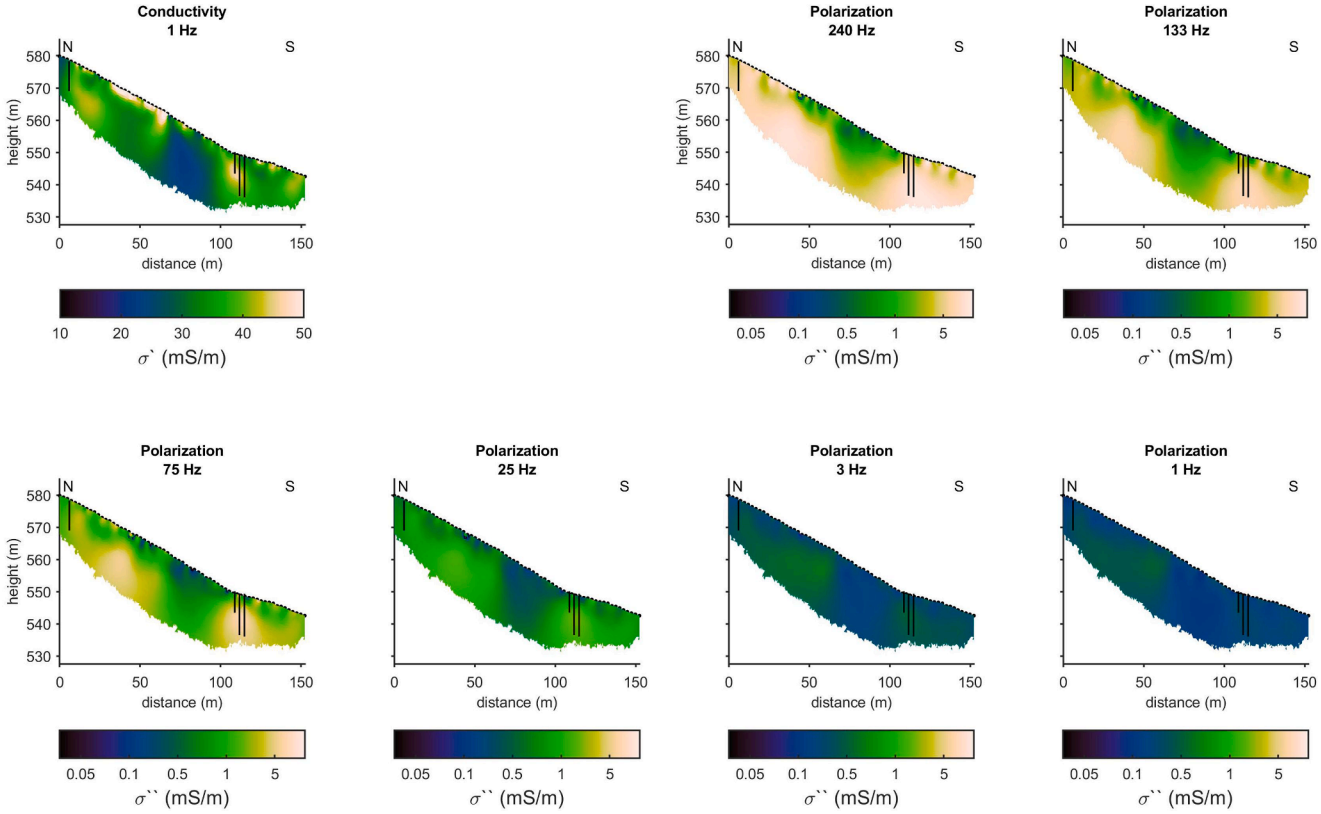

Fig. 4. Inversion results for FDIP data collected along line L1 expressed in terms of the real (σ') and imaginary (σ'') components of the complex conductivity. The conductivity results are consistent across all frequencies in the measured range (0.25–240 Hz) and we present only the conductivity image for data collected at 1 Hz; whereas polarization images are presented for data collected at different frequencies. We use a different color map to present the FDIP imaging results considering the larger dynamic in the polarization values than resolved in TDIP. The black points in each image represent the electrodes at the surface. The vertical lines imposed in plots of L1 indicate the position and maximum depth reached with the DPH. The plots have a vertical exaggeration 2:1 to better identify subsurface changes at depth.

the charges coating the EDL than coarser grains, where the charges need to move across larger distances (i.e., Revil and Florsch 2010). Measurements in sands have revealed a stronger polarization response around 1 Hz (e.g., Koch et al., 2011); while the increase in the polarization with increasing the frequency has also been reported from laboratory measurements in clayey materials (e.g., Leroy and Revil, 2009), supporting our interpretation regarding the increase in the σ'' values.

A potential plane of instability has been identified at a depth fluctuating around 10 m bgs based on the DPH data (see Stumvoll et al., 2022). In their study, the geometry of such plane was only interpolated between three DPH soundings. In contrasts, the FDIP images provide quasi-continuous information about the depth to such plane across the entire slope. In particular, the variations in the depth of the potential plane of instability can be easily observed in the polarization image at 240 Hz corresponding to the contact to the high polarization values (σ'' > 5 mS/m). Such plane of instability is close to the surface at both ends of the profile, while a depth of ca. 12 m can be resolved to the center of the profile, between 60 and 90 m approximately.

Although it is associated with larger acquisition times (see Table 1), SIP results presented in Fig. 4 clearly resolve the frequency-dependence of the polarization, with these images revealing an increase in the values at high frequencies. The low polarizable anomaly resolved through TDIP, FDIP and SIP, is presumably dominated by coarse grains as indicated by its low conductivity and polarization. Accordingly, the anomalous area (between 60 and 90 m profile distance) may permit the accumulation of water, either due to infiltration from the surface or groundwater flow from northern areas along the top soil layer. Such water cannot easily flow downhill (i.e., towards south), due to the increase in clay materials in the polarizable anomaly. Thus, this polarizable anomaly (found at ca 100 m profile distance associated to high clay contents) ise a relevant subsurface feature controlling surface deformation, considering that the accumulation of groundwater in such area may, in turn, result in the increase in pore pressure.

3.3. The frequency dependence of the SIP measurements

Grain size distributions obtained through laboratory analysis of soil samples retrieved at the Hofermuehle site report a high silt (varying between 20 and 50 %) and clay (varying between 6 and 25 %) content (Stumvoll et al., 2022). Such analysis also revealed that the fine grains (silt and clays) comprise 70 % of the materials above 4 m bgs and about 40 % between 4 and 6 m depth (c.f. Fig. 1). In Fig. 5, we present the measured spectra for all samples extracted from wells BK1 and BK3 located at 44 m and 125 m, respectively, along the FDIP profile (see Fig. 1). In general, the spectra reveal a similar trend with low polarization values in the range between 1 and 10 Hz, and higher values with increasing the frequency. The resolved peaks observed at in the range between ca. 200 and 600 Hz suggest that the measurements are not dominated by EM coupling, which is commonly related to a linear increase with increasing the frequency (Hallof, 1974; Pelton et al., 1978). Moreover, in Fig. 5, it is possible to observe a peak (i.e., critical frequency) in the polarization around 1000 Hz for samples with the highest clay content (>15 %); while the peak is observed around 200 Hz for lower clay contents. We also observe that high clay contents (>10 %) are also related to higher polarization values; although no clear trend is observed for the conductivity values. Nevertheless, sediments in BK1 (downhill) reveal also the lowest σ'' values for the samples with high clay content, clearly evidencing the high heterogeneity of the study area and stressing the relevance of field-scale investigations. The Cole-Cole parameters fitted to the measured spectra revealed only a weak correlation with the dominating grain size and are not discussed in this study. Thus, we believe that not only the grain size controls the frequency-dependence, but other textural parameters are critical, such as the pore size (e.g., Binley et al., 2005).

The analysis of multiple-salinity measurements and application of Eq. (13) results in estimations of formation factor (F) varying between 4.24 and 10.83, while the values for the cementation exponent (m) were found to be between 1.68 and 3.26, as presented in Table 3. The values obtained through our laboratory analysis are consistent to other laboratory observations (see Weller et al., 2015 and references therein). In particular, for the Hofermuehle, we can see that F increases in samples taken from the deeper areas, where soil samples reveal an increasing content of gravels. However, m and F values need to be taken with caution, as we may have unintentionally changed the geometry of the pore space during the preparation of the SIP columns in the laboratory. As mentioned above, we dried the sample before mixing it with the brine

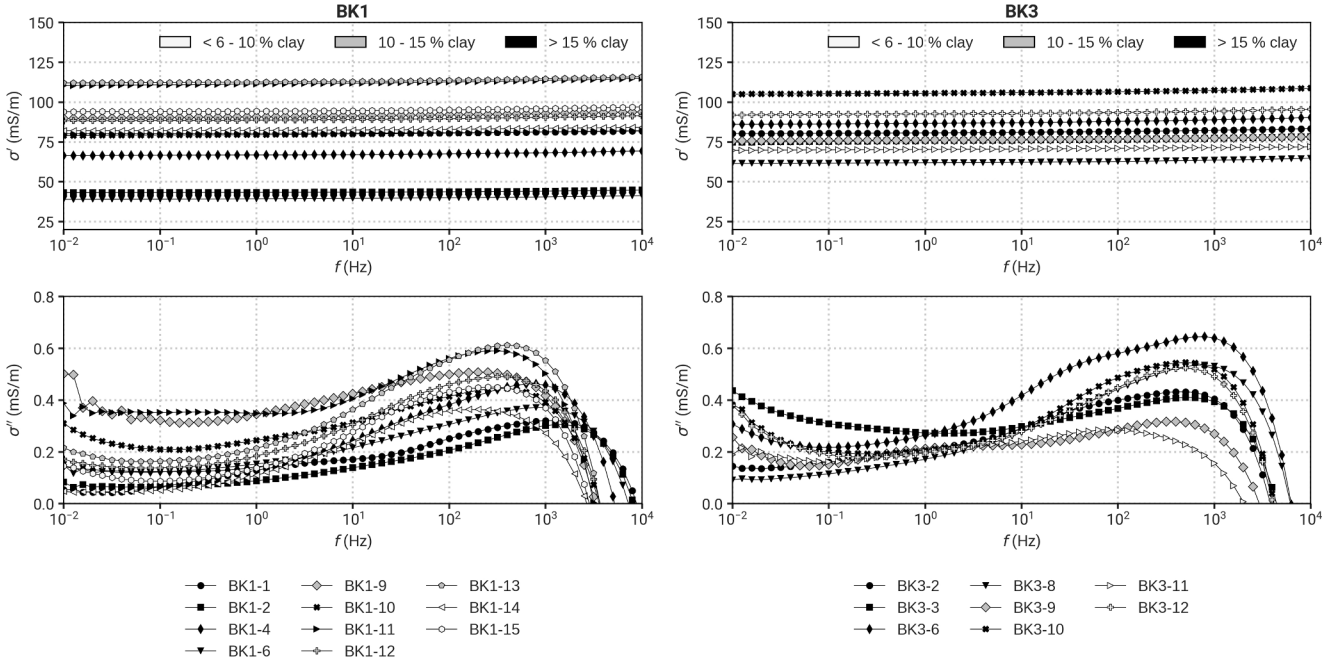

Fig. 5. Frequency-dependence of the complex conductiviy for SIP data collected in the soil samples recovered from boreholes BK1 and BK3. Different symbols aim at aiding in the identification of spectra measured for samples taken at different depths. The color-coded spectra aim at identifying samples with variable clay content.

Table 3
Laboratory SIP results of fully-saturated soil samples – at a given porosity (Φ) - after varying the fluid conductivity to obtain the formation factor (F), the cementation exponent (m) and the real component of the surface conductivity (σ_s').

Sample	F(–)	σ_s' (mS/m)	Φ (%)	m (–)	Description
BK1-2	4.24	43.67	47	1.9	Clay/Silt
BK1-10	4.94	146.43	39	1.68	Silt/Sand
BK1-12	10.83	144.22	48	3.26	Silt/Gravel
BK1-13	7.23	117.68	–	–	Silt/Gravel

to fill the column, with such steps repeated for the different salinities. While we took extra care to maintain the porosity constant along our measurements, we cannot neglect changes in the packing of the samples, i.e., in the connectivity between pores, which is the key factor controlling m. Accordingly, as the σ'_s, m, and F obtained from Eq. (13) may be influenced due to changes in the interconnected porosity while filling the column, they may not reflect the field conditions.

The comparison with the imaging results shows that the laboratory analysis presented in Fig. 5 confirms the polarization response increase with the clay content. Moreover, the presented spectra evidence a f_c above 100 Hz, consistent to the increase in σ'' observed in our field results. Fig. 5 also confirms the low polarization values ($\sigma'' < 0.5$ mS/m) in the frequency range between 0.25 and 5 Hz, which was also resolved in both the FDIP and the TDIP data. The observed increase in the polarization response at frequencies below 0.1 Hz in our laboratory measurements is also similar to the one reported by Leroy and Revil (2009), which was explained by the membrane polarization. Such low frequencies require several hours to be collected, especially for imaging configurations; thus, they are not suited for field-scale measurements and we will not discuss them further.

To better quantify the frequency-dependence of the σ^* of the field SIP data, we present in Fig. 6 the Cole-Cole parameters (Eq. (4)) describing the frequency-dependence observed in SIP imaging results. The Cole-Cole model was fitted pixel-wise to the inversion obtained for data collected between 1 and 60 Hz, considering that higher frequencies may be related to possible Maxwell-Wagner polarization (e.g., Revil and Florsch, 2010) and EM-coupling (e.g., Flores Orozco et al., 2013; 2018a; 2021). Plots in Fig. 6 reveal patterns in the images of Cole-Cole parameters that are consistent with those also described before for TDIP and FDIP. Hereafter we will only discuss the DC-conductivity (σ_0) and the normalized chargeability (M_n) considering that both parameters are required for the estimation of hydraulic conductivity (see Eqs. (6) and (7)). The σ_0 presented in Fig. 6 is equivalent to the conductivity obtained through traditional ERT surveys, and obviously shows similar patterns and values as the σ' images computed from TDIP and FDIP data (Figs. 3 and 4). Likewise, the normalized chargeability illustrated in Fig. 6 quantifies the polarization response obtained from multi-frequency SIP data and shows features consistent to the σ'' images. Such observation demonstrates the good quality of all data sets presented and the possibility to obtain similar results from TDIP, FDIP and SIP data. Quantitatively, we can see that the normalized chargeability resolved through SIP has values ranging between 1 and 1.5 mS/m; while the values in the σ'' reach a maximum of 5 mS/m for inversion of FDIP data collected at 240 Hz, and below 0.5 mS/m for both FDIP data collected at 1 Hz and TDIP images.

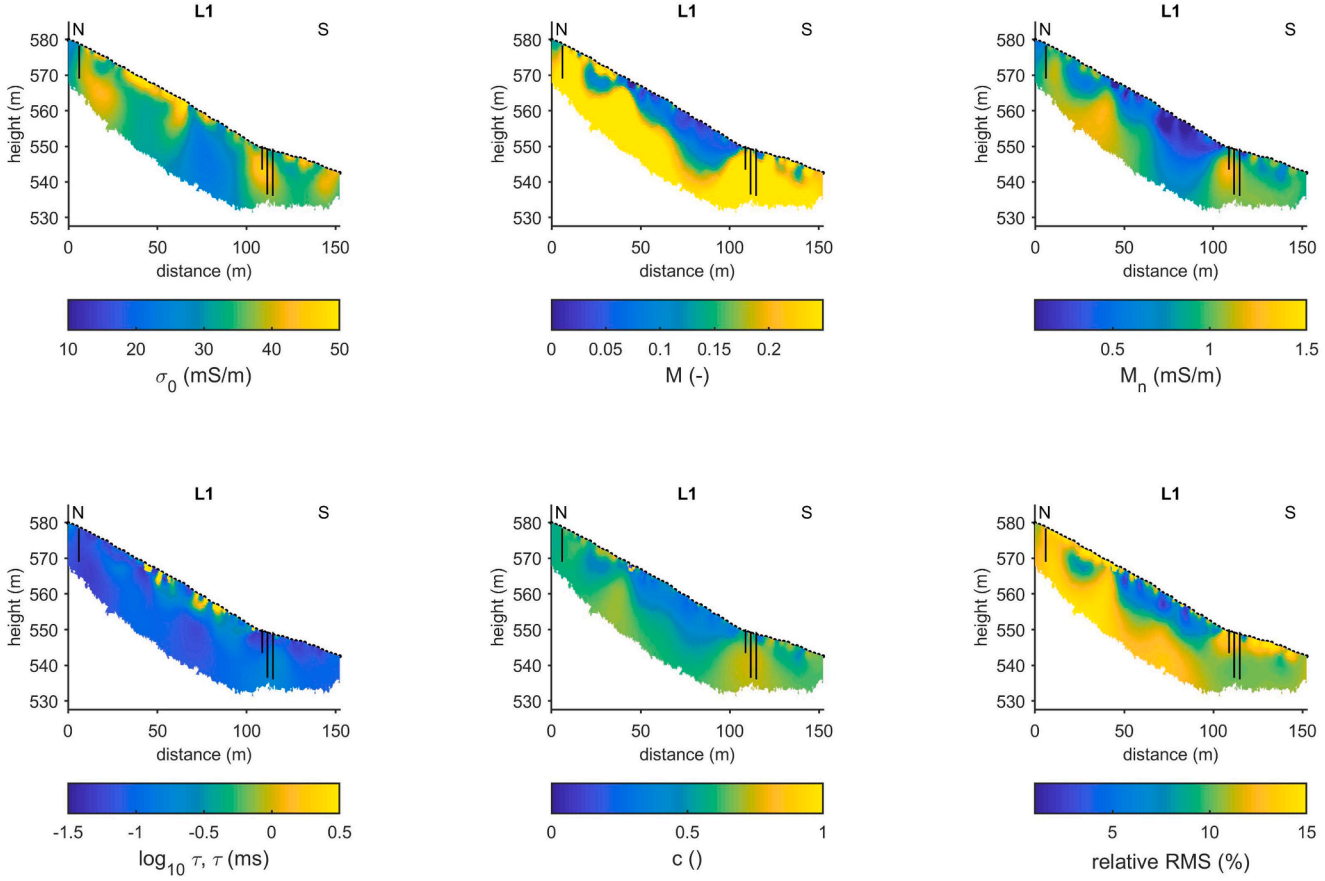

Fig. 6. Plots of the Cole-Cole parameter fitted to the imaging results obtained after the inversion of SIP data collected along L1. The vertical lines imposed in the plots indicate the position and maximum depth reached with the DPH. The plots have a vertical exaggeration 2:1 to better identify subsurface changes at depth.

3.4. Joint inversion of electrical resistivity and seismic refraction tomography

We have proposed an interpretation of the complex conductivity results and their frequency dependence. However, the use of other geophysical methods could help to shed light on the lateral variation observed within the σ^* interpreted as variations in the clay content. Seismic methods are primarily sensitive to variations in the density and thus offer the opportunity to map variations within the weathered materials as well as the contact to the bedrock. Moreover, seismic images can also help to delineate possible changes within the Flysch that may point to possible fractures as an alternative interpretation of the σ^* images. To avoid the interpretation of independently resolved electrical and seismic models, we present in Fig. 7 the results obtained through the joint inversion of the two data sets, namely P-wave travel times and resistivity data.

Fig. 7 reveals, as expected, negligible changes in the images resolved for σ_0 and σ_∞, and both models are consistent with the σ' inverted from TDIP, FDIP data (also with σ_0 from SIP) as well as in the same range of values from laboratory measurements. The V_p clearly resolves two layers: (1) the unconsolidated materials related to low values ($V_p <$ 1000 m/s) on top, with a thickness varying between 5 and 10 m; and (2) the weathered rocks characterized by higher velocity values ($V_p >$ 2000 m/s) on the bottom layer. A third layer may be suggested at larger depth associated to velocities above 2200 m/s, which may reflect a contrast to less weathered materials. The joint inversion results do not extend to the same depth as the TDIP imaging results and cannot resolve the contact to the bedrock. This is due to the limited extension of the seismic survey as well as the filtering of deep measurements in the resistivity data caused by poor reciprocity in the phase readings (as described for the processing of the SIP data).

Due to the lack of deep resistivity readings, the subsurface model resolved through the joint inversion scheme reflects the layering sensed by the seismic method, which is less sensitive to variations in the textural properties of the materials than the IP measurements. Accordingly, the V_p model reveals only the two layers corresponding to the unconsolidated materials and the weathered materials, with the interface between both likely resolved by the 2200 m/s isoline. Hence, spatial variations in this isoline are related to the geometry of the plane of instability. Moreover, the conductivity images presented in Fig. 7 also resolve the lateral variations within the top layer, with low seismic velocity values (~1000 m/s) between 60 and 90 m, in agreement with the conductivity and polarization anomalies observed in TDIP and FDIP images. However, the V_p model does not reveal any lateral variation within the bottom layer that may indicate possible fractures, supporting the interpretation that low polarizable anomalies in TDIP, FDIP and SIP images are likely related to changes in the textural properties.

The joint inversion solves directly for water saturation (S_w) and porosity (Φ), two relevant parameters for landslide characterization. Fig. 7 shows a high water saturation (>60 %) across the entire image plane, with the lowest areas close to the surface, in agreement with the shallow groundwater level (ca. 1 m bgs) as presented in Table 3. The lowest water saturation (≤60 %) is resolved within the anomalous region, between 60 and 90 m profile distance and close to the surface, where the highest air saturation (>25 %) is resolved. The highest porosity (ca 60 %) is observed in the top layer corresponding to the unconsolidated sediments, with the maximum values observed between 60 and 90 m distance. The weathered rocks unit reveals porosity values ranging between 30 and 40 %.

In case of the joint inversion results presented here, the impedance

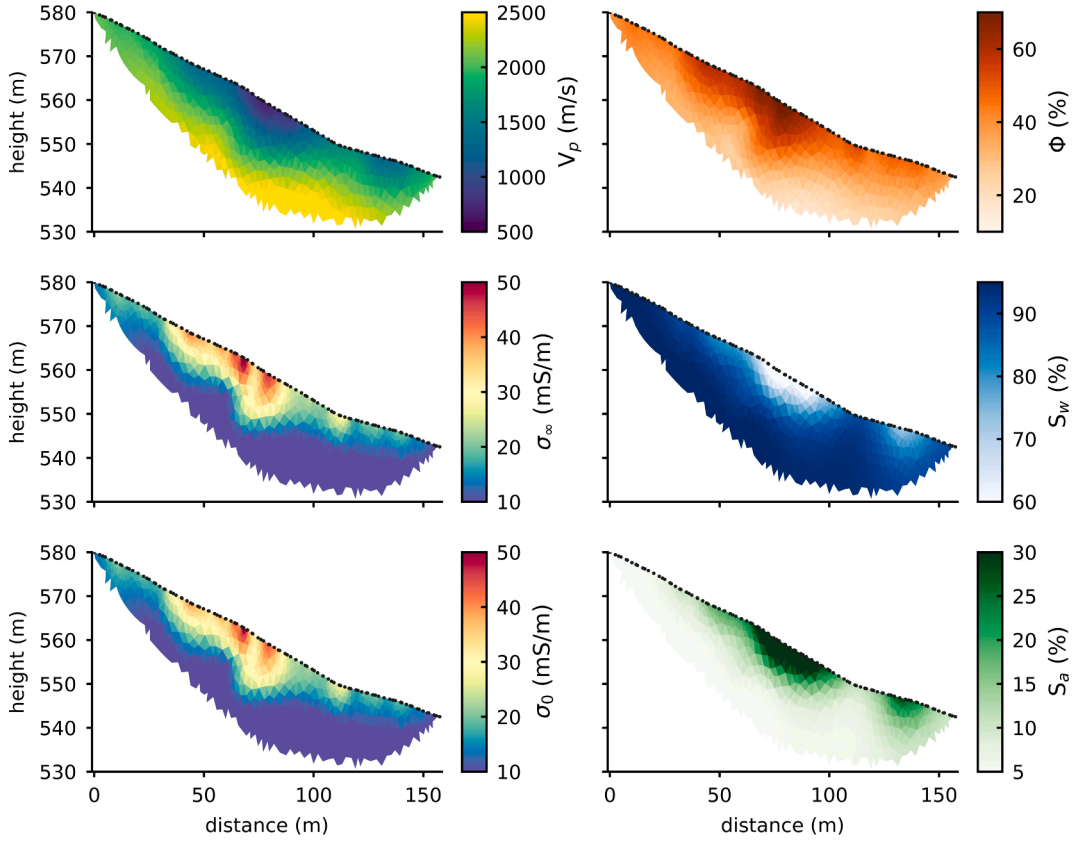

Fig. 7. Imaging results obtained from the joint inversion of electrical resistivity and seismic refraction tomography expressed in terms of the geophysical parameters, i.e. the seismic velocity of the P-waves (V_p) and the electrical conductivity at low and high frequency (σ_0 and σ_∞). The joint inversion directly resolves for relevant hydrogeological parameters: here expressed in terms of the water saturation (S_w), air saturation (S_a) and porosity (Φ). The black dots on the top of the plots represent the position of the electrodes as well as the geophones and shot points. All plots are oriented North – South.

phase values are disregarded and we only use the transfer resistances (at high and low frequencies) as model parameters. Although computed without involving the IP readings, the images of water content and porosity provide consistent structures and confirm the geometry of both the plane of instability and the anomaly between 60 and 90 m distance resolved through TDIP, FDIP and SIP images. Such anomaly corresponds to the lowest porosity and water content, supporting the interpretation of unsaturated materials with lower clay content described above for the IP images. Besides supporting the interpretation of the IP images, the resolved porosity model can be used to obtain the formation factor (Eq. (3)), which is critical for estimating the hydraulic conductivity (see Weller et al., 2015).

4. Discussion

4.1. Quantification of the hydraulic conductivity based on different IP methods

In this study, subsurface information at different scales has been gained through TDIP, FDIP and SIP investigations, permitting the interpretation of a plane of instability between the unconsolidated materials and the weathered Flysch, with a depth varying between 1 and 5 m across the slope. The contact to the bedrock is resolved through TDIP images at depths below 12 m, with some lateral variations (especially to the south). Such contacts are in agreement with results of previous investigations at the site based on DPH (Stumvoll et al., 2022) as well as with variations in the V_p values obtained from the inversion of SRT data. Moreover, to the center of the images, we can observe an anomaly of low polarization which we interpret as an area of low clay content within both the unsaturated materials and the weathered Flysch. The imaging results presented earlier reveal the complexity of the study area where the thickness and textural properties of the units might suddenly change in a few meters.

So far, the interpretation of the TDIP, FDIP and joint inversion results have pointed to variations in the clay content and, thus, we have inferred lateral variations in the hydraulic properties of the subsurface at the Hofermuehle site. However, no hydrogeological information is available at the site. To overcome this and provide a quantitative interpretation of the IP results, we decided to apply the petrophysical models proposed by Weller et al. (2015) linking IP parameters and the hydraulic conductivity. Fig. 8a and 8b present the estimations after applying the $K-\sigma''$ relationship presented in Eq. (6). For σ'' we use inversion results resolved at 1 Hz obtained from both the linearly converted TDIP (Fig. 8a) and the FDIP (Fig. 8b) measurements collected at profile L1.

As discussed during the interpretation of the imaging results above, the top unit represents the unconsolidated materials related to high K values ($>10^{-5}$ m/s), as expected due to their poor compaction. The unit below corresponds to weathered Flysch, with K values $\sim 10^{-5}$ m/s estimated from TDIP, and slightly lower values from FDIP data ($K \sim 10^{-}$

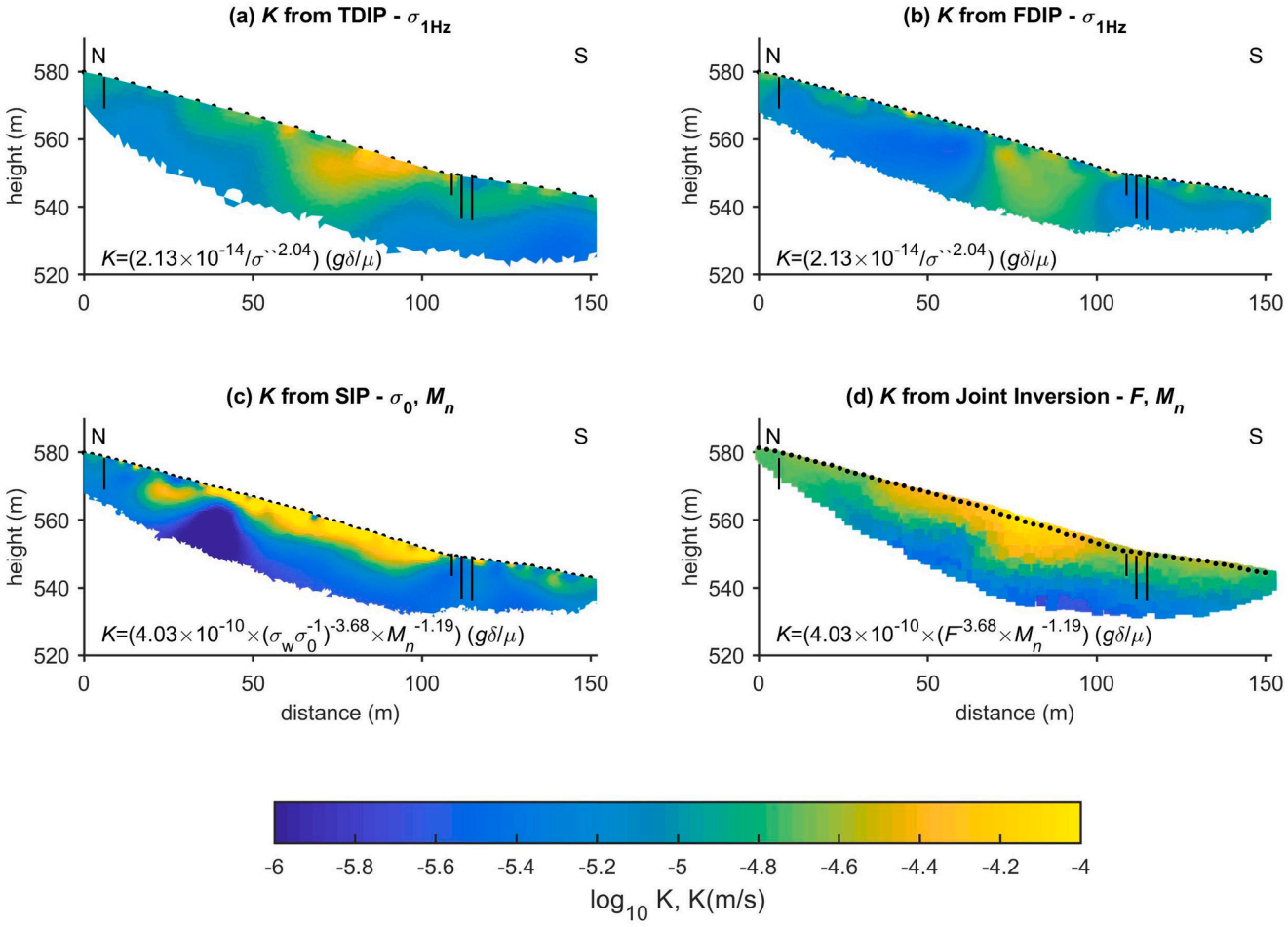

Fig. 8. Estimated values of hydraulic conductivity (K) from the inverted TDIP, FDIP and SIP data collected along line L1. The first row presents estimations using the link between K and the σ'' at 1 Hz obtained from (a) TDIP, and (b) FDIP imaging results. The second row presents the results using the relationship between K and the normalized chargeability (M_n), as obtained from: (c) fitting the Cole-Cole model to SIP data, and (d) the joint inversion results. For the formation factor (F), we used σ_0 as a first approximation for SIP data, while porosity models are used to compute F for the joint inversion results. To allow a better visual comparison, the TDIP image was only plotted to a distance of 150 m that is the maximum length of the FDIP profile. All plots are presented in a 1:1 aspect ratio.

$^{5.5}$ m/s). Considering the smaller electrode spacing (see Table 1), and thus, higher resolution, we believe that the FDIP provides a better estimate of K for the unconsolidated and the weathered materials than the TDIP images. The bedrock is resolved only in the TDIP images revealing much lower hydraulic conductivity ($<10^{-5.5}$ m/s), as expected for clay-rich consolidated materials (in this case from the Flysch formation). The highest K values can be observed in the before mentioned anomaly between 60 and 90 m profile distance, supporting our interpretation of low clay content. The agreement in the values and structures demonstrates that both measuring techniques (TDIP and FDIP) provide quantitatively similar results. The cut-off frequency in the system used for the collection of TDIP hindered any analysis if the full-wave form (e.g., Fiandaca et al., 2012; 2013).

Although promising, the $K-\sigma''$ model presented in Eq. (6) disregards the frequency-dependence observed in the electrical properties at the field- (Fig. 4) and laboratory-scale (Fig. 5). Alternatively, we can use the obtained Cole-Cole parameters (i.e., M_n and σ_0) in the Eq. (7) to obtain the hydraulic conductivity image presented in Fig. 8c. The K-M_n estimations are consistent with those resolved through a single frequency (i.e., σ''_{1Hz}), with high values ($10^{-4.5}$ m/s) close to the surface at both ends of the profile corresponding to the unsaturated, unconsolidated materials. Fig. 8c reveals the highest K values ($\leq 10^{-4}$ m/s) close to the surface, between 40 and 110 m along the imaging plane. Although such anomaly is also observed in the $K-\sigma''$ images (i.e., Fig. 8a and 8b), the hydraulic conductivity values are higher in Fig. 8c and extended over a broader area. This discrepancy highlights the advantage of SIP surveys, which is sensitive to subsurface variations captured in a broad frequency range. Thus, the information gained through SIP measurements provides insight into subsurface heterogeneities that might not be resolved entirely through single frequency IP data.

We note here, that in order to solve for the same range of hydraulic conductivity values through single- and multi-frequency IP data, we had to modify the first experimental parameter in Eq. (7) from 4.03×10^{-9} to 4.03×10^{-10}. This slight change is likely related to the lack of accurate measurements of the formation factor for field-scale SIP measurements. In case of Fig. 8c, we used an approximation (i.e., $F = \frac{\sigma_f}{\sigma_0}$), which neglects the contribution of σ'_s to the formation factor. In this regard, the Eq. (6) linking $K-\sigma''_{1Hz}$ offer the advantage that does not require any information about F. Nonetheless, the consistency observed between Fig. 8a, 8b and 8c demonstrates the applicability to our data of the experimental models proposed by Weller et al. (2015) .

4.2. Independent quantification of the hydraulic conductivity through a joint inversion scheme

Both resistivity and seismic refraction tomography are commonly used methods in landslide investigations (Jongmans and Garambois, 2007; Hibert et al., 2012; Uhlemann et al., 2016; Pazzi et al., 2019; Whiteley et al., 2019). Thus, in this study we decided to investigate the joint inversion of data coming from both techniques. Employing the joint inversion we can obtain the electrical conductivity, porosity, and thus the formation factor in an imaging framework. The latter is linked to the effective porosity and, as mentioned by Weller et al. (2015), is a critical parameter for estimating the hydraulic conductivity from electrical data sets. Fig. 8d presents the estimations using Eq. (8), yet based on the M_n and F obtained from the joint inversion. We can observe that in general the hydraulic conductivity patterns are consistent with those resolved through SIP measurements (Fig. 8c). We argue that such consistency demonstrates the ability to obtain a good approximation on the hydraulic conductivity at the field scale either through TDIP, FDIP and SIP imaging as well as through the proposed ERT-SRT joint inversion approach deployed here. We believe such evaluation is fair considering that K-estimations presented in Fig. 8 are computed using completely different data and inversion approaches (SIP data vs ERT-SRT).

In general, the analysis of only conductivity data at low and high frequencies lacks the resolution required to assess variations in the polarization response that can only be retrieved through TDIP, FDIP or SIP measurements. Consequently, the IP has emerged as an important method in hydrogeological investigations (Revil and Florsch, 2010; Binley et al., 2015; Revil et al., 2020). However, the incorporation of a different source of data in the joint inversion scheme, such as the variations in the seismic velocities, provides subsurface information that cannot be resolved through conductivity images. In particular, joint inversion results resolve for minimal changes for both σ_0 and σ_∞ images in the weathered materials; thus, a low M_n value (see Eq. (5)), which is inconsistent with those resolved through SIP. However, the improved estimation of F through the joint inversion accounting for the increase in the V_p (and the decrease in the porosity) balances the lack of information regarding variations in M_n, thus, permitting to resolve for consistent K values in comparison with those obtained through SIP.

We have argued that hydraulic conductivity estimations based on the SIP imaging method, as presented in Fig. 8c, can be evaluated through the K estimations obtained by means of the joint inversion results presented in Fig. 8d. The lack of direct measurements of K at the study area limits a more rigorous evaluation. However, samples recovered from BK1 and BK3 were analyzed in the lab to quantify the gravimetric water content (c.f., Fig. 1), which can be used to evaluate the estimations resolved through the joint inversion. The volumetric water content (Θ) measured in soil samples fluctuates around 0.4, which is in agreement with the values obtained through the joint inversion. The soil samples reveal large variations in samples collected between 2 and 4 m depth for both grain size and (especially) the gravimetric water content. Such variations cannot be solved through the smooth-constrained algorithm used in this study (i.e., for either IP or the joint inversion). For instance, Θ obtained from gravimetric water content (assuming a constant density of 1300 km m^3) vary between 0.1 and 0.6; whereas our inversions resolve only for changes between 0.3 and 0.5. The changes observed in the laboratory data might be related to the characteristics of the samples (e.g., volume) and only provide information at the sampling location. Additionally, the discrepancies can be also explained considering that the calculation of water volumetric constant assumes a constant soil density although variations in the materials at depth are clear (see Fig. 1). Accordingly, the lack of spatial resolution hinders the assessment of changes across the slope; thus, highlighting the advantage of the geophysical imaging techniques presented, namely SIP or the joint inversion.

To extend our analysis, we also investigated the applicability of the relationship proposed by Revil et al. (2020) linking K with σ_∞ and M_n presented in Eq. (11). We used the parameters obtained after fitting the Cole-Cole model to the SIP data (see Fig. 6); however, estimations resulted in negative K values. It means that $\sigma_\infty < (M_n/R)$ in Eq. (11), for $R = 0.1$ (as provided by Revil et al., 2020). In our case, M_n is fitted independently to the SIP inversion results and no constraint is imposed; thus, resulting in values that render Eq. (11) inappropriate for our data. The direct inversion of the M and $\sigma_\infty$from the primary and secondary voltages measured in the TDIP data as proposed by Soueid Ahmed and Revil (2018) warranties the computation of parameters that fulfill the petrophysical model underlying in Eqs. (11) and (12).

Instead of fitting a Cole-Cole model, Revil et al. (2021) estimate the normalized chargeability from the imaginary conductivity, using a linear approximation (i.e., $\sigma'' \propto M_n$). In Fig. 9, we present plots of the M_n as a function of the σ'', with the latter obtained from the inversion of the data collected at 6 Hz, which is the data set closest to the geometric mean of the frequency range used to fit the Cole-Cole parameters (between 1 and 60 Hz). As observed in Fig. 9, σ'' increases with increasing M_n; however, the values are spread over a wider range and it is not possible to obtain a linear correlation between both parameters. In Fig. 9, we also impose the linear correlation using the equation proposed by Revil et al. (2020), demonstrating that such relationship is not applicable to our data. Nevertheless, Fig. 7 demonstrates that positive water content can be solved through the joint inversion, which

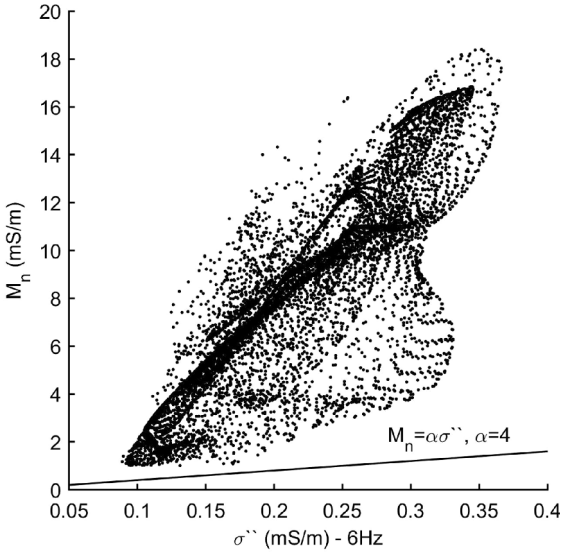

Fig. 9. Plots of the normalized chargeability (M_n) fitted to SIP imaging results and the imaginary conductivity (σ'') after the inversion of the data collected at 6 Hz. Such frequency represents the closest one to the geometric mean between the minimum (1 Hz) and maximum (60 Hz) frequencies fitted with the Cole-Cole model for the hydraulic conductivity estimations. The solid line indicates the linear model proposed by Revil et al. (2020) to link both quantities.

incorporates the dynamic Stern layer model (Eqs. (8)–(10)), and the petrophysical model in Eq. (12) linking Θ to σ_∞ and M_n. This is achieved due to the volume conservation constraint honored during parameter estimation to ensure that the volumetric fractions of soil, water and air equal unity (e.g., Wagner et al., 2019).

The joint inversion algorithm used here is based on the Timur equation linking porosity and P-wave velocities (see Wagner et al., 2019 for further details). However, such approximation may be limited in unsaturated materials, where V_p is not only controlled by changes in density, but also due to interprarticle stress and in-pore pressure (e.g., Shen et al. 2016). The Timur equation does not consider such effects and may mislead the inverted porosity values, and thus the K-estimations, especially for low velocities (e.g., $V_p < 800$ m/s) in the unsaturated clayey materials (see Hibert et al., 2012; Uhlemann et al., 2016). The incorporation of resistivity data may help to correct the porosity estimations in the joint inversion, yet future research requires evaluating the use of a different petrophysical model, for instance the Hertz-Mindlin theory (see Shen et al., 2016). Moreover, further research should also consider the extension of the joint-inversion to directly solve for the elastic properties by including S-wave or surface waves data (see Hibert et al., 2012; Uhlemann et al., 2016 and references therein). Including such measurements, may permit for an improved estimation of porosity, moisture content and thus, the hydraulic conductivity.

4.3. 3D subsurface model of study area

To fully exploit the TDIP data collected at the Hofermuehle site, we present in Fig. 10 a visualization of the hydraulic conductivity as obtained from the 3D inversion of the six TDIP lines. Accordingly, we do not present an interpolation of the 2D images, but an actual subsurface 3D model that simultaneously fits data collected in all lines in terms of the complex conductivity, which is then transformed to K using Eq. (3). The advantage of collecting mapping (i.e., 3D) data is that it allows to investigate spatial variations in the electrical and hydraulic properties of the landslides. The 3D inversion is recommended to improve the consistency between the obtained results for the data collected in each line. As expected from the Fig. 3, the 3D model resolves minimal changes in the West-East direction, but is mainly dominated by the North-South variations in the central part of the investigated area. In particular, Fig. 10 reveals the potential of a 3D model to accurately delineate the geometry of the poor drainage area identified in the Southern part of the landslide.

The lateral variations in subsurface properties resolved through the geophysical models, and the estimated variations in porosity and K, demonstrate a poor hydraulic connectivity between the North and South sections of our profile and may be a first step to explain the large changes in the water level recorded within the piezometers (between 1 and 3 m bgs) on the Northern and Southern part of the investigation area (see Table 2). We need to consider that the model proposed by Weller et al. (2015) was developed for fully saturated samples, limiting its applicability in the top layer at the Hofermuehle site, consisting of not fully saturated sediments (see Table 2). Accordingly, the extension of the experimental parameters in Eqs. (6) and (7) for estimating K in not fully saturated materials requires further investigation. Further investigations also need to consider 3D SIP measurements, where we can resolve the frequency-dependence as well as the spatial variations of the electrical properties of the subsurface.

5. Conclusions

We used geophysical methods to investigate the Hofermuehle landslide in two steps. First, we conducted a mapping with TDIP to cover extensive areas in short acquisition times. Second, we carried out measurements with SRT and multi-frequency FDIP. Inversion results for TDIP and FDIP data generally reveal low conductivity and polarization values in areas close to the surface, corresponding to the unconsolidated materials, while higher values are resolved below corresponding to clay-rich materials from the Flysch formation. For FDIP data, we resolve a layer with a thickness of ca. 8 m corresponding to weathered material with a polarization response that increases with increasing the frequency. The bedrock reveals the higher polarization response; however, this is only resolved in TDIP data, due to the longer electrode spacing and profile length used for the data collection. Thus, we have no information about the frequency-dependence of the Flysch materials in the bedrock. There is a clear discontinuity in the center of our geophysical profiles characterized by low values of σ' and σ'' which we interpret as materials with lower clay content than those on the North and South sections of our profile.

The use of a petrophysical model, derived from laboratory investigations, permitted the estimation of the hydraulic conductivity in an imaging framework from TDIIP and FDIP data. The hydraulic conductivity images permitted to delineate a preferential flow path corresponding to high K values in the central part of the IP profiles, where the lowest polarization values were observed. Lower K values ($<10^{-5}$ m/s) are resolved downhill to the South, indicating a possible area where groundwater may accumulate. SIP images are consistent to those obtained through TDIP and FDIP data, but reveal a significant frequency dependence, with the higher σ'' values observed at high frequencies (>60 Hz). Such frequency-dependence is also observed in laboratory measurements of soil samples. Although the K images are consistent between SIP and TDIP (and FDIP at 1 Hz), the former reveal a higher contrast in the resolved values and a slight variation in the geometry of the unit. Hence, hydraulic conductivity estimations based on a single frequency may not fully reveal subsurface heterogeneities, which can only be resolved through the collection of SIP data.

The seismic refraction data permitted the delineation of the contact between unconsolidated material and the weathered Flysch, corresponding to contrasting values in the velocity of the P-waves (V_p) in agreement with the vertical variations in IP images. The application of an algorithm inverting resistivity and seismic data permitted the consistent estimation of K with those obtained by means of the SIP method. We argue that both approaches are independent and can be applied to evaluate the results presented. The joint inversion algorithm neglects the IP response and it is only controlled by variations in σ' and

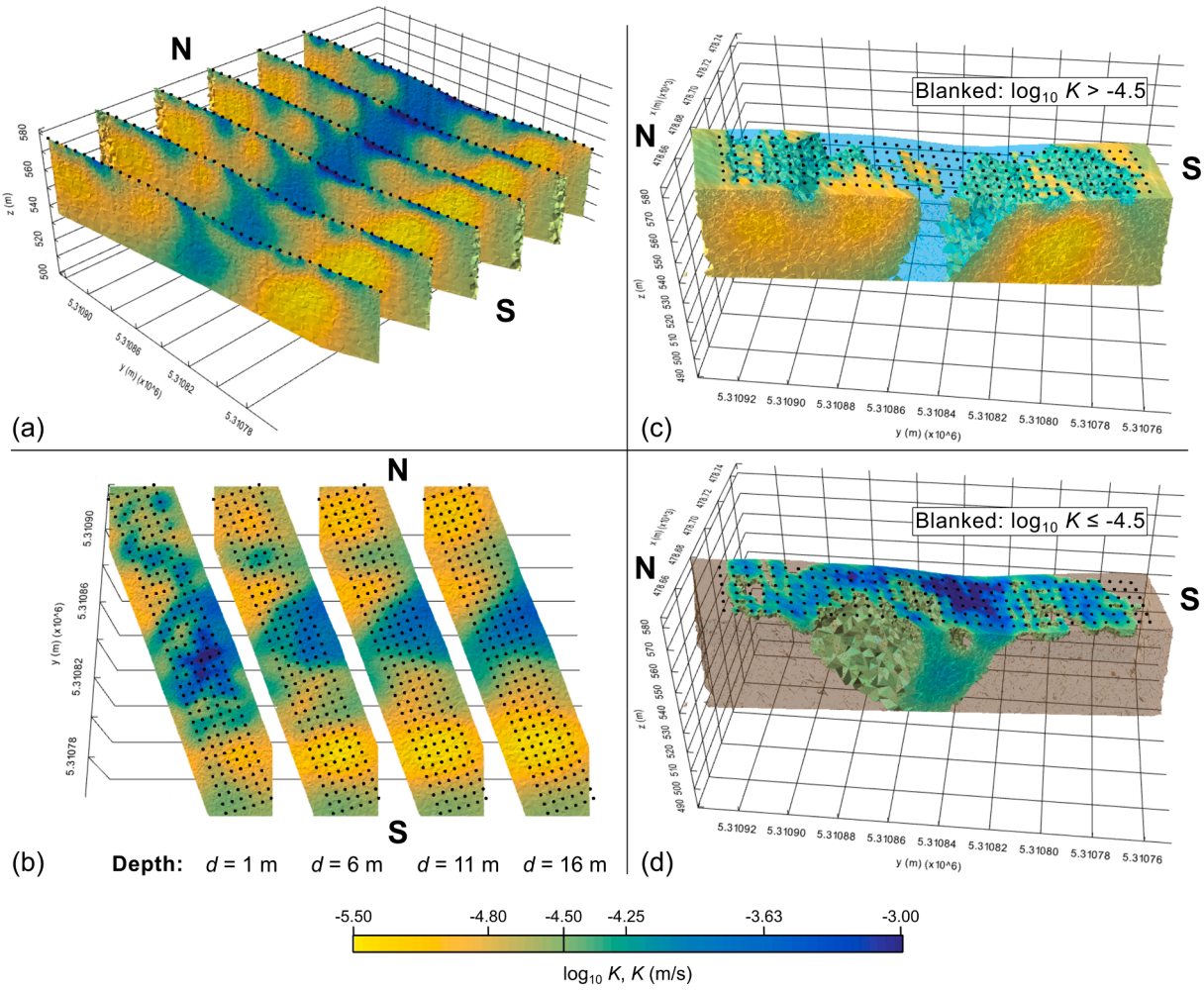

Fig. 10. 3D inversion results of TDIP data expressed in terms of the hydraulic conductivity (K). The dots on top of the plots indicate the position of the electrodes. All plots are oriented North-South.

V_p; thus permitting an improved estimation of the F and K. On the opposite, estimations based on M_n in our study are mainly controlled by the frequency of the IP response, which is then used to fit Cole-Cole parameters compute the hydraulic conductivity. Our results demonstrate that IP imaging permits delineating areas of poor-drainage (i.e., low K) in the subsurface where groundwater may accumulate, which is commonly a precondition for land sliding.

Declaration of Competing Interest

The authors declare that they have no known competing financial interests or personal relationships that could have appeared to influence the work reported in this paper.

Data availability

Data will be made available on request.

Acknowledgements

This research has been supported by the Swiss National Science Foundation (grant no. 200021L_178823). The authors acknowledge TU Wien Bibliothek for financial support through its Open Access Funding Programme.

References

Abdulsamad, F., Revil, A., Ahmed, A.S., Coperey, A., Karaoulis, M., Nicaise, S., Peyras, L., 2019. Induced polarization tomography applied to the detection and the monitoring of leaks in embankments. Eng. Geol. 254, 89–101.

Archie, G.E., 1942. The electrical resistivity log as an aid in determining some reservoir characteristics. Trans. AIME 146 (01), 54–62.

Bairlein, K., Hördt, A., Nordsiek, S., 2014. The influence on sample preparation on spectral induced polarization of unconsolidated sediments. Near Surf. Geophys. 12 (5), 667–678.

Bell, R., Glade, T., Granica, K., Heiss, G., Leopold, P., Petschko, H., Pomaroli, G., Proske, H. and Schweigl, J., 2013. Landslide susceptibility maps for spatial planning in lower Austria. In: Landslide Science and Practice. Springer, Berlin, Heidelberg, pp. 467–472.

Bichler, A., Bobrowsky, P., Best, M., Douma, M., Hunter, J., Calvert, T., Burns, R., 2004. Three-dimensional mapping of a landslide using a multi-geophysical approach: the Quesnel Forks landslide. Landslides 1 (1), 29–40.

Binley, A., Kemna, A., 2005. DC resistivity and induced polarization methods. In: Hydrogeophysics. Springer, Dordrecht, pp. 129–156.

Binley, A., Slater, L., 2020. Resistivity and induced polarization: Theory and applications to the near-surface earth. Cambridge University Press.

Binley, A., Slater, L.D., Fukes, M., Cassiani, G., 2005. Relationship between spectral induced polarization and hydraulic properties of saturated and unsaturated sandstone. Water Resour. Res. 41 (12).

Binley, A., Hubbard, S.S., Huisman, J.A., Revil, A., Robinson, D.A., Singha, K., Slater, L. D., 2015. The emergence of hydrogeophysics for improved understanding of subsurface processes over multiple scales. Water Resour. Res. 51 (6), 3837–3866.

Binley, A., Keery, J., Slater, L., Barrash, W., Cardiff, M., 2016. The hydrogeologic information in cross-borehole complex conductivity data from an unconsolidated conglomeratic sedimentary aquifer. Geophysics 81 (6), E409–E421.

Blanchy, G., Saneiyan, S., Boyd, J., McLachlan, P., Binley, A., 2020. ResIPy, an intuitive open source software for complex geoelectrical inversion/modeling. Comput. Geosci. 137, 104423.

Börner, F.D., Schopper, J.R., Weller, A., 1996. Evaluation of transport and storage properties in the soil and groundwater zone from induced polarization measurements1. Geophys. Prospect. 44 (4), 583–601.
Cassiani, G., Kemna, A., Villa, A., Zimmermann, E., 2009. Spectral induced polarization for the characterization of free-phase hydrocarbon contamination of sediments with low clay content. Near Surf. Geophys. 7 (5–6), 547–562.
Chambers, J.E., Wilkinson, P.B., Kuras, O., Ford, J.R., Gunn, D.A., Meldrum, P.I., Pennington, C.V.L., Weller, A.L., Hobbs, P.R.N., Ogilvy, R.D., 2011. Three-dimensional geophysical anatomy of an active landslide in Lias Group mudrocks, Cleveland Basin, UK. Geomorphology 125 (4), 472–484.
Dahlin, T., Leroux, V., 2012. Improvement in time-domain induced polarization data quality with multi-electrode systems by separating current and potential cables. Near Surf. Geophys. 10 (6), 545–565.
Damm, B., Terhorst, B., 2010. A model of slope formation related to landslide activity in the Eastern Prealps, Austria. Geomorphology 122 (3–4), 338–350.
Danielsen, J.E., Auken, E., Jørgensen, F., Søndergaard, V., Sørensen, K.I., 2003. The application of the transient electromagnetic method in hydrogeophysical surveys. J. Appl. Geophys. 53 (4), 181–198.
Fiandaca, G., Auken, E., Christiansen, A.V., Gazoty, A., 2012. Time-domain-induced polarization: Full-decay forward modeling and 1D laterally constrained inversion of Cole-Cole parameters. Geophysics 77 (3), E213–E225.
Fiandaca, G., Ramm, J., Binley, A., Gazoty, A., Christiansen, A.V., Auken, E., 2013. Resolving spectral information from time domain induced polarization data through 2-D inversion. Geophys. J. Int. 192 (2), 631–646.
Flores Orozco, A., Kemna, A., Oberdörster, C., Zschornack, L., Leven, C., Dietrich, P., Weiss, H., 2012b. Delineation of subsurface hydrocarbon contamination at a former hydrogenation plant using spectral induced polarization imaging. J. Contam. Hydrol. 136, 131–144.
Flores Orozco, A., Kemna, A., Zimmermann, E., 2012a. Data error quantification in spectral induced polarization imaging. Geophysics 77 (3), E227–E237.
Flores Orozco, A., Williams, K.H., Kemna, A., 2013. Time-lapse spectral induced polarization imaging of stimulated uranium bioremediation. Near Surf. Geophys. 11 (5), 531–544.
Flores Orozco, A., Bücker, M., Steiner, M., Malet, J.P., 2018a. Complex-conductivity imaging for the understanding of landslide architecture. Eng. Geol. 243, 241–252.
Flores Orozco, A., Gallistl, J., Bücker, M., Williams, K.H., 2018b. Decay curve analysis for data error quantification in time-domain induced polarization imaging. Geophysics 83 (2), E75–E86.
Flores Orozco, A., Aigner, L., Gallistl, J., 2021. Investigation of cable effects in spectral induced polarization imaging at the field scale using multicore and coaxial cables. Geophysics 86 (1), E59–E75.
Gallistl, J., Weigand, M., Stumvoll, M., Ottowitz, D., Glade, T., Flores Orozco, A., 2018. Delineation of subsurface variability in clay-rich landslides through spectral induced polarization imaging and electromagnetic methods. Eng. Geol. 245, 292–308.
Gance, J., Malet, J.P., Supper, R., Sailhac, P., Ottowitz, D., Jochum, B., 2016. Permanent electrical resistivity measurements for monitoring water circulation in clayey landslides. J. Appl. Geophys. 126, 98–115.
Glover, P., 2009. What is the cementation exponent? A new interpretation. The Leading Edge 28 (1), 82–85.
Glover, P.W., 2017. A new theoretical interpretation of Archie's saturation exponent. Solid Earth 8 (4), 805–816.
Hallof, P.G., 1974. The IP phase measurement and inductive coupling. Geophysics 39 (5), 650–665.
Hibert, C., Grandjean, G., Bitri, A., Travelletti, J., Malet, J.P., 2012. Characterizing landslides through geophysical data fusion: Example of the La Valette landslide (France). Eng. Geol. 128, 23–29.
Hördt, A., Blaschek, R., Kemna, A., Zisser, N., 2007. Hydraulic conductivity estimation from induced polarisation data at the field scale—the Krauthausen case history. J. Appl. Geophys. 62 (1), 33–46.
Jongmans, D., Garambois, S., 2007. Geophysical investigation of landslides: a review. Bulletin de la Société géologique de France 178 (2), 101–112.
Kemna, A., 2000. Tomographic Inversion of Complex Resistivity: Theory and Application. Der Andere Verlag Osnabrück, Germany.
Kemna, A., Binley, A., Slater, L., 2004. Crosshole IP imaging for engineering and environmental applications. Geophysics 69 (1), 97–107.
Kemna, A., Binley, A., Cassiani, G., Niederleithinger, E., Revil, A., Slater, L., Williams, K. H., Flores Orozco, A., Haegel, F.H., Hördt, A., Kruschwitz, S., 2012. An overview of the spectral induced polarization method for near-surface applications. Near Surf. Geophys. 10 (6), 453–468.
Koch, K., Kemna, A., Irving, J., Holliger, K., 2011. Impact of changes in grain size and pore space on the hydraulic conductivity and spectral induced polarization response of sand. Hydrol. Earth Syst. Sci. 15 (6), 1785–1794.
Lacroix, P., Handwerger, A.L., Bièvre, G., 2020. Life and death of slow-moving landslides. Nat. Rev. Earth Environ. 1 (8), 404–419.
Lapenna, V., Lorenzo, P., Perrone, A., Piscitelli, S., Sdao, F., Rizzo, E., 2003. High-resolution geoelectrical tomographies in the study of Giarrossa landslide (southern Italy). Bull. Eng. Geol. Environ. 62 (3), 259–268.
Lapenna, V., Lorenzo, P., Perrone, A., Piscitelli, S., Rizzo, E., Sdao, F., 2005. 2D electrical resistivity imaging of some complex landslides in Lucanian Apennine chain, southern Italy. Geophysics 70 (3), B11–B18.
Leroy, P., Revil, A., 2009. A mechanistic model for the spectral induced polarization of clay materials. J. Geophys. Res. Solid Earth 114 (B10).
Lesmes, D.P., Friedman, S.P., 2005. Relationships between the electrical and hydrogeological properties of rocks and soils. In: Hydrogeophysics. Springer, Dordrecht, pp. 87–128.
Lesmes, D.P., Frye, K.M., 2001. Influence of pore fluid chemistry on the complex conductivity and induced polarization responses of Berea sandstone. J. Geophys. Res. Solid Earth 106 (B3), 4079–4090.
Lima, P., Steger, S., Glade, T., Tilch, N., Schwarz, L., Kociu, A., 2017. May. Landslide susceptibility mapping at national scale: a first attempt for Austria. In: Workshop on World Landslide Forum. Springer, Cham, pp. 943–951.
Linde, N., Binley, A., Tryggvason, A., Pedersen, L.B., Revil, A., 2006. Improved hydrogeophysical characterization using joint inversion of cross-hole electrical resistance and ground-penetrating radar traveltime data. Water Resour. Res. 42 (12).
López-Sánchez, M., Mansilla-Plaza, L., 2017. Geometric factor and influence of sensors in the establishment of a resistivity-moisture relation in soil samples. J. Appl. Geophys. 145, 1–11.
Maierhofer, T., Hauck, C., Hilbich, C., Kemna, A., Flores-Orozco, A., 2022. Spectral induced polarization imaging to investigate an ice-rich mountain permafrost site in Switzerland. The Cryosphere 16 (5), 1903–1925.
Marescot, L., Monnet, R., Chapellier, D., 2008. Resistivity and induced polarization surveys for slope instability studies in the Swiss Alps. Eng. Geol. 98 (1–2), 18–28.
Martin, T., Günther, T., Flores Orozco, A., Dahlin, T., 2020. Evaluation of spectral induced polarization field measurements in time and frequency domain. J. Appl. Geophys. 180, 104141.
Mellage, A., Holmes, A.B., Linley, S., Vallée, L., Rezanezhad, F., Thomson, N., Gu, F., Van Cappellen, P., 2018. Sensing coated iron-oxide nanoparticles with spectral induced polarization (SIP): experiments in natural sand packed flow-through columns. Environ. Sci. Technol. 52 (24), 14256–14265.
Mollaret, C., Wagner, F.M., Hilbich, C., Scapozza, C., Hauck, C., 2020. Petrophysical joint inversion applied to alpine permafrost field sites to image subsurface ice, water, air, and rock contents. Front. Earth Sci. 8, 85.
Pazzi, V., Morelli, S., Fanti, R., 2019. A review of the advantages and limitations of geophysical investigations in landslide studies. Int. J. Geophys.
Pelton, W.H., Ward, S.H., Hallof, P.G., Sill, W.R., Nelson, P.H., 1978. Mineral discrimination and removal of inductive coupling with multifrequency IP. Geophysics 43 (3), 588–609.
Perrone, A., Lapenna, V., Piscitelli, S., 2014. Electrical resistivity tomography technique for landslide investigation: a review. Earth Sci. Rev. 135, 65–82.
Petschko, H., Bell, R., Leopold, P., Heiss, G., Glade, T., 2013. Landslide inventories for reliable susceptibility maps in Lower Austria. In: Landslide Science and Practice. Springer, Berlin, Heidelberg, pp. 281–286.
Promper, C., Glade, T., 2016. Multilayer-exposure maps as a basis for a regional vulnerability assessment for landslides: applied in Waidhofen/Ybbs, Austria. Nat. Hazards 82 (1), 111–127.
Revil, A., 2012. Spectral induced polarization of shaly sands: Influence of the electrical double layer. Water Resour. Res. 48 (2).
Revil, A., 2013. Effective conductivity and permittivity of unsaturated porous materials in the frequency range 1 mHz–1GHz. Water Resour. Res. 49 (1), 306–327.
Revil, A., Coperey, A., Shao, Z., Florsch, N., Fabricius, I.L., Deng, Y., Delsman, J.R., Pauw, P.S., Karaoulis, M., De Louw, P.G.B., van Baaren, E.S., 2017. Complex conductivity of soils. Water Resour. Res. 53 (8), 7121–7147.
Revil, A., Ahmed, A.S., Coperey, A., Ravanel, L., Sharma, R., Panwar, N., 2020. Induced polarization as a tool to characterize shallow landslides. J. Hydrol. 589, 125369.
Revil, A., Florsch, N., 2010. Determination of permeability from spectral induced polarization in granular media. Geophys. J. Int. 181 (3), 1480–1498.
Revil, A., Schmutz, M., Abdulsamad, F., Balde, A., Beck, C., Ghorbani, A., Hubbard, S.S., 2021. Field-scale estimation of soil properties from spectral induced polarization tomography. Geoderma 403, 115380.
Rücker, C., Günther, T., Wagner, F.M., 2017. pyGIMLi: An open-source library for modelling and inversion in geophysics. Comput. Geosci. 109, 106–123.
Sen, P.N., Scala, C., Cohen, M.H., 1981. A self-similar model for sedimentary rocks with application to the dielectric constant of fused glass beads. Geophysics 46 (5), 781–795.
Shen, J., Crane, J.M., Lorenzo, J.M., White, C.D., 2016. Seismic velocity prediction in shallow (< 30 m) partially saturated, unconsolidated sediments using effective medium theory. J. Environ. Eng. Geophys. 21 (2), 67–78.
Sidle, R., Ochiai, H., 2006. Processes, prediction, and land use. Water Resources Monograph, American Geophysical Union, Washington.
Slater, L., 2007. Near surface electrical characterization of hydraulic conductivity: From petrophysical properties to aquifer geometries—A review. Surv. Geophys. 28 (2), 169–197.
Slater, L.D., Glaser, D.R., 2003. Controls on induced polarization in sandy unconsolidated sediments and application to aquifer characterization. Geophysics 68 (5), 1547–1558.
Slater, L., Lesmes, D.P., 2002. Electrical-hydraulic relationships observed for unconsolidated sediments. Water Resour. Res. 38 (10), 31–41.
Soueid Ahmed, A., Revil, A., 2018. 3-D time-domain induced polarization tomography: a new approach based on a source current density formulation. Geophys. J. Int. 213 (1), 244–260.
Steger, S., Brenning, A., Bell, R., Glade, T., 2016. The propagation of inventory-based positional errors into statistical landslide susceptibility models. Nat. Hazards Earth Syst. Sci. 16 (12), 2729–2745.
Steiner, M., Wagner, F.M., Maierhofer, T., Schöner, W., Flores Orozco, A., 2021. Improved estimation of ice and water contents in Alpine permafrost through constrained petrophysical joint inversion: The Hoher Sonnblick case study. Geophysics 86 (5), 1–84.
Steiner, M., Katona, T., Fellner, J., Flores Orozco, A., 2022. Quantitative water content estimation in landfills through joint inversion of seismic refraction and electrical resistivity data considering surface conduction. Waste Manage. 149, 21–32.

Stumvoll, M.J., Canli, E., Engels, A., Thiebes, B., Groiss, B., Glade, T., Schweigl, J., Bertagnoli, M., 2020. The "Salcher" landslide observatory—experimental long-term monitoring in the Flysch Zone of Lower Austria. Bull. Eng. Geol. Environ. 79 (4), 1831–1848.

Stumvoll, M.J., Schmaltz, E.M., Glade, T., 2021. Dynamic characterization of a slow-moving landslide system–assessing the challenges of small process scales utilizing multi-temporal TLS data. Geomorphology 389, 107803.

Stumvoll, M.J., Schmaltz, E.M., Kanta, R., Roth, H., Grall, B., Luhn, J., Flores-Orozco, A., Glade, T., 2022. Exploring the dynamics of a complex, slow-moving landslide in the Austrian Flysch Zone with 4D surface and subsurface information. Submitted to Catena.

Supper, R., Ottowitz, D., Jochum, B., Kim, J.H., Römer, A., Baron, I., Pfeiler, S., Lovisolo, M., Gruber, S., Vecchiotti, F., 2014. Geoelectrical monitoring: an innovative method to supplement landslide surveillance and early warning. Near Surf. Geophys. 12 (1), 133–150.

Tarasov, A., Titov, K., 2013. On the use of the Cole-Cole equations in spectral induced polarization. Geophys. J. Int. 195 (1), 352–356.

Travelletti, J., Sailhac, P., Malet, J.P., Grandjean, G., Ponton, J., 2012. Hydrological response of weathered clay-shale slopes: Water infiltration monitoring with time-lapse electrical resistivity tomography. Hydrol. Process. 26 (14), 2106–2119.

Uhlemann, S., Hagedorn, S., Dashwood, B., Maurer, H., Gunn, D., Dijkstra, T., Chambers, J., 2016. Landslide characterization using P-and S-wave seismic refraction tomography—The importance of elastic moduli. J. Appl. Geophys. 134, 64–76.

Ustra, A., Slater, L., Ntarlagiannis, D., Elis, V., 2012. Spectral induced polarization (SIP) signatures of clayey soils containing toluene. Near Surf. Geophys. 10 (6), 503–515.

Wagner, F.M., Mollaret, C., Günther, T., Kemna, A., Hauck, C., 2019. Quantitative imaging of water, ice and air in permafrost systems through petrophysical joint inversion of seismic refraction and electrical resistivity data. Geophys. J. Int. 219 (3), 1866–1875.

Weigand, M., Kemna, A., 2016. Relationship between Cole-Cole model parameters and spectral decomposition parameters derived from SIP data. Geophys. J. Int. 205 (3), 1414–1419.

Weller, A., Slater, L., Binley, A., Nordsiek, S., Xu, S., 2015. Permeability prediction based on induced polarization: Insights from measurements on sandstone and unconsolidated samples spanning a wide permeability range. Geophysics 80 (2), D161–D173.

Whiteley, J.S., Chambers, J.E., Uhlemann, S., Wilkinson, P.B., Kendall, J.M., 2019. Geophysical monitoring of moisture-induced landslides: a review. Rev. Geophys. 57 (1), 106–145.

Zisser, N., Kemna, A., Nover, G., 2010. Relationship between low-frequency electrical properties and hydraulic permeability of low-permeability sandstones. Geophysics 75 (3), E131–E141.